Marine Geoscience and Energy Resources 193 (2026) 207863

Contents lists available at ScienceDirect

Marine Geoscience and Energy Resources

journal homepage: www.sciencedirect.com/journal/marine-geoscience-and-energy-resources

DInSAR kinematics and long-term dynamics of Mesijune salt fountain in the Zagros Mountains. Terrestrial analogue for the development of supra-namakier and marginal namakier-dammed basins

Francisco Gutiérrez [a,*], Mahmud Haghshenas Haghighi [b], Issa Ilyati [c], Mahdi Motagh [d], Miren del Val [e], Michael R. Hudec [f], Eduard Roca [g], Guillermo Pérez-Villar [a]

[a] Department of Earth Sciences, University of Zaragoza, Spain
[b] Institute of Photogrammetry and GeoInformation, Leibniz University Hannover, Germany
[c] Department of Earth Sciences, Shiraz University, Iran
[d] GFZ Helmholtz Centre for Geosciences at Postdam, Germany
[e] Centro Nacional de Investigación sobre la Evolución Humana (CENIEH), Burgos, Spain
[f] Bureau of Economic Geology, Jackson School of Geosciences, The University of Texas at Austin, Box X, Austin, TX, 78713-8924, USA
[g] UB-GEOMODELS Research Institute, Department of Geodynamics and Geophysics, University of Barcelona, Barcelona, Spain

ARTICLE INFO

Keywords:
Salt tectonics
Salt extrusion
Salt sheet
Autosuture
Namakier
Sentinel-1

ABSTRACT

The morphologically degraded Mesijune salt extrusion (137 km^2, 650 m local relief), with a summit dome and a multidirectional namakier, is the largest salt fountain in the Zagros Mountains. This work analyses the long-term evolution of the salt extrusion, including the development of associated basins, and characterises its current kinematics with decomposed DInSAR data. The salt fountain displays an alluvium-filled supra-namakier basin associated with an encircling autosuture located downstream of an obstacle of upturned bedrock strata (probable flap). This basin atop the namakier expanded downstream as the salt sheet advanced downslope and experienced rotation, resulting in a sedimentary fill with a general offlap arrangement and backtilted structure. In the Late Pleistocene, the advancing namakier front obstructed drainage creating a marginal namakier-dammed basin with lacustrine-palustrine deposits dated by Optically Stimulated Luminiscence (OSL) at 14.3 ± 2.5 ka. Currently, the highest horizontal displacement rates (140 mm/yr) occur in the steep flanks of the summit dome, and progressively decrease to null values towards the stable fronts of the namakiers. The summit dome is dominated by surface lowering at an average rate of -16 mm/yr, suggesting that it could vanish in around 5 kyr, involving the transition of the salt fountain into salt droplet. The comparison of LOS displacement time series with monthly rainfall data from a nearby station indicates steady salt creep unaffected by the rainfall regime. The Mesijune salt fountain may serve as a terrestrial analogue for unravelling the past evolution of salt sheets and associated features from the geological record.

1. Introduction

Salt diapirs can play a fundamental role on key elements of hydrocarbon, geothermal, and even ore hydrothermal systems, exerting a significant control over migration pathways, reservoir development and the formation of traps and seals for fluids (Warren, 2006; Leach et al., 2010; Jackson and Hudec, 2017; Perona et al., 2018; Duffy et al., 2023; Zhang and Alves, 2024). The common relationships between diapiric salt structures and fluid systems, such as hydrocarbon reservoirs andore deposits (e.g., Zn-Pb), are largely related to two essential properties of rock salt. First, the extremely low permeability of crystalline salt. According to Warren (2017), salt is the best geological seal, a condition that can be maintained over tens of millions of years, although it can be degraded by long-term stability issues. This sealing capacity is related not only to the intrinsic zero transmissivity of crystalline salt, but also to its self-healing capability. Despite the fact that evaporites constitute <2% of the earth's sedimentary rocks, 14 of the world's 25 largest oil fields and 9 of the world's 25 largest gas fields are sealed by

* Corresponding author.
E-mail addresses: fgutier@unizar.es (F. Gutiérrez), mahmud@ipi.uni-hannover.de (M.H. Haghighi), isaq24@yahoo.com (I. Ilyati), mahdi.motagh@gfz.de (M. Motagh), miren.delval@cenieh.es (M. del Val), michael.hudec@beg.utexas.edu (M.R. Hudec), eduardroca@ub.edu (E. Roca).

https://doi.org/10.1016/j.marger.2026.207863
Received 10 April 2026; Received in revised form 13 June 2026; Accepted 29 July 2026
Available online 30 July 2026
3117-5775/© 2026 The Authors. Published by Elsevier Ltd. This is an open access article under the CC BY license (http://creativecommons.org/licenses/by/4.0/).

evaporites (Warren, 2016). Second, the negligible yield strength of rock salt, which enables it to flow under low differential stress, giving rise to salt structures with a wide range of geometries. This rheology allows salt to flow and spread laterally at the surface, forming salt sheets emplaced atop previously formed sediments and rocks. These allochthonous sheets can be very extensive and may form canopies when they coalesce with other allochthonous salt bodies (Hudec and Jackson, 2006). Such structures are of particular interest in geological resource exploration and exploitation (e.g., hydrocarbon reservoirs, geostorage, geothermal energy; O'Brien and Lerche, 1988; Raymond et al., 2022; Duffy et al., 2023). Recent investigations also suggest that salt sheets may be favourable settings for hypogene karst. Salt dissolution caused by rising groundwater from an underlying aquifer may result in hazardous subsidence severely affecting human structures (e.g., Elda salt sheets in the Betics of southern Spain; Tomás et al., 2026).

Salt sheets and canopies can reach kilometre-scale thickness and may control sedimentation patterns. Rapidly subsiding salt-expulsion basins (i.e., minibasins) can form atop salt sheets, that may be transported downslope, experience rotation, and eventually become encapsulated within impermeable salt (Hudec et al., 2009; Canova et al., 2025a). The topography created by advancing salt sheets can guide sediment flux as well as thickness and facies changes. The frontal oversteepened slopes of salt sheets are prone to mass wasting processes (Hudec et al., 2009). The distribution and advance of salt can also distort sediment transport paths (e.g., deflection, blockage), and exert some control on the distribution of sedimentation zones and the associated facies (Booth et al., 2003; Canova et al., 2025b).

The kinematics and geometry (shape, thickness, and lateral extent) of allochthonous salt sheets are primarily controlled by the amount of salt supplied by the feeders, the rate of salt dissolution at the surface, the development of protecting residual and aggradational covers (e.g., Bruthans et al., 2009), the topography over which the salt advances, and the erosional or depositional regime of the environment in which the salt sheet develops. It is also influenced, although to a lesser extent, by the nature of the materials onto which the salt is emplaced. Where these are water-saturated unconsolidated sediments, the advancing salt may generate overpressure conditions that reduce the effective shear strength of the subsalt sediments. This reduction in effective shear strength can encourage rapid basal sliding, promoting the advance of salt sheets and resulting in more laterally extensive salt bodies.

In subsiding marine sedimentary basins (aggradational environments), the salt expelled through a feeder typically advances by a combination of spreading and gliding mechanisms over poorly consolidated sediments. The base of these salt sheets typically climbs outward through a series of flats and ramps, controlled by the relative rates of salt advance versus sediment accumulation (Hudec and Jackson, 2006; Hearon IV et al., 2015; Rowan et al., 2020; Cofrade et al., 2023; Canova et al., 2025b). In these submarine settings, degradation of the salt sheet by dissolution tends to be rather slow because of two factors: (1) accumulation of a mantle of protecting deposits on the salt; and (2) reduced halite dissolution capability of sea water compared with fresh water. For these reasons, submarine salt sheets and canopies can extend up to hundreds of kilometres and reach kilometre-scale thickness (e.g., Gulf of Mexico).

Extrusive salt sheets in terrestrial environments show significant differences with those emplaced in marine environments due to a number of factors: (1) the orifice of the feeders may be located on topographic highs (e.g., anticlinal ridges) and the salt sheets may advance over steep terrain, resulting in salt extrusions with high overall gradient; (2) salt lobes typically advance down more frictional bedrock (Talbot, 1979) or over porous deposits that are unlikely to be affected by overpressure conditions, with impact on the advance mechanisms (e.g., frontal rolling versus gliding); (3) dissolutional weathering and erosion play a much more important role, affecting the thickness, degradation and persistence of salt sheets; (4) bedrock reliefs can play a key role on salt flow patterns (e.g., lateral confinement, obstruction, deflection, separation) and may control the development of supra-salt and near-salt sedimentary environments.

Salt sheets and canopies formed in subaqueous environments, with higher preservation potential, are those that typically constitute the seals for large hydrocarbon reservoirs and the ones that have received greater attention. Their investigation and characterisation has been mainly carried out using subsurface data (seismic reflection data, boreholes) and, to a lesser extent, examples found in the exposed rock record, where stratigraphic and structural relationships in the associated sediments have allowed the reconstruction of their development. Salt sheets formed in terrestrial environments are rarely preserved in the stratigraphic record, unless they have developed in rapidly subsiding basins where they have been rapidly buried (e.g., Cofrade et al., 2023). Their investigation generally requires different approaches, including the analysis of currently active salt extrusions from a geological and geomorphological perspective as illustrated by this work.

The semiarid Fars Arc of the Zagros Mountains constitutes the most remarkable natural laboratory for the study of active subaerial salt extrusions worldwide, including salt fountains comprising a summit dome above a feeder and lateral spreading salt sheets, also known as namakiers (based on *namak*, the Farsi word for salt) (Talbot and Jarvis, 1984; Jahani et al., 2007). This work analyses the long-term evolution and current kinematics of the Mesijune salt fountain (Fig. 1). The salt extrusion is located in the SW Fars Arc, in an area with a mean temperature of 14°C and an average annual precipitation of 174 mm/yr (2000-2024 record at Mazayjen-Zarindast station 26-315 of the Iranian Meteorological Organization, around 20 km WNW of Mesijune; lat. of 28.058°, long. of 54.647°). The Mesijune salt extrusion has been selected for this study because of a number of outstanding features, including: (1) it is the largest salt fountain in the region (137 km^2) (2) it displays a multidirectional namakier (i.e., radial spreading); instead of the typical uni- or bi-directional namakiers; (3) the salt fountain, dominated by fluvial landscape and external drainage, is currently in a mature and degraded evolutionary stage; (4) bedrock obstacles have significantly influenced salt flow on short- and long-term scales, resulting in the development of supra-namakier and namakier-dammed basins in a terrestrial environment, documented for the first time in this work.

The main aims of this investigation include: (1) unravelling the long-term evolution of a salt fountain and its interaction with obstructing relief, including the novel finding of a supra-namakier basin associated with an autosuture and a namakier-dammed marginal paleolake basin; (2) characterising for the first time the current DInSAR kinematics of a degrading salt fountain transitioning into a salt droplet; and (3) integrating long- and short-term data, reconstructing and predicting the evolution of the salt extrusion. The results obtained contribute to better understanding aspects of the behaviour of the poorly investigated salt sheets developed in terrestrial environments, that are difficult to analyse using subsurface data or ancient analogues.

2. Geological setting

The Mesijune diapir is located in the NW-SE-trending Zagros Fold-and-Thrust Belt, an orogen resulting from the oblique convergence between the Arabian and Eurasian plates during the Late Cretaceous and Cenozoic (Stöklin, 1968; Ricou et al., 1977; Agard et al., 2011; Orang et al., 2017) (Fig. 1A). This convergence led to the closure of the Neo-Tethys Ocean and continues to the present day, as demonstrated by GPS data indicating ongoing N-S plate convergence at a rate of 20-25 mm/yr (Vernant et al., 2004). The Zagros developed southwest of the Arabia-Eurasia suture (Stöklin, 1968) along the pre-existing Late Permain-late Turonian Arabia passive margin of the Neo-Tethys. It is a thin-skinned fold-and-thrsut belt detached along Upper Proterozoic and Miocene evaporitic units, and comprises two longitudinal structural zones to the SW of the Main Zagros Reverse Fault, which defines the Arabia-Eurasia suture (Stöklin, 1968) (Fig. 1A): (1) the High Zagros (or Imbricated Belt) on the NE, and (2) the Simply Folded Belt on the SW,

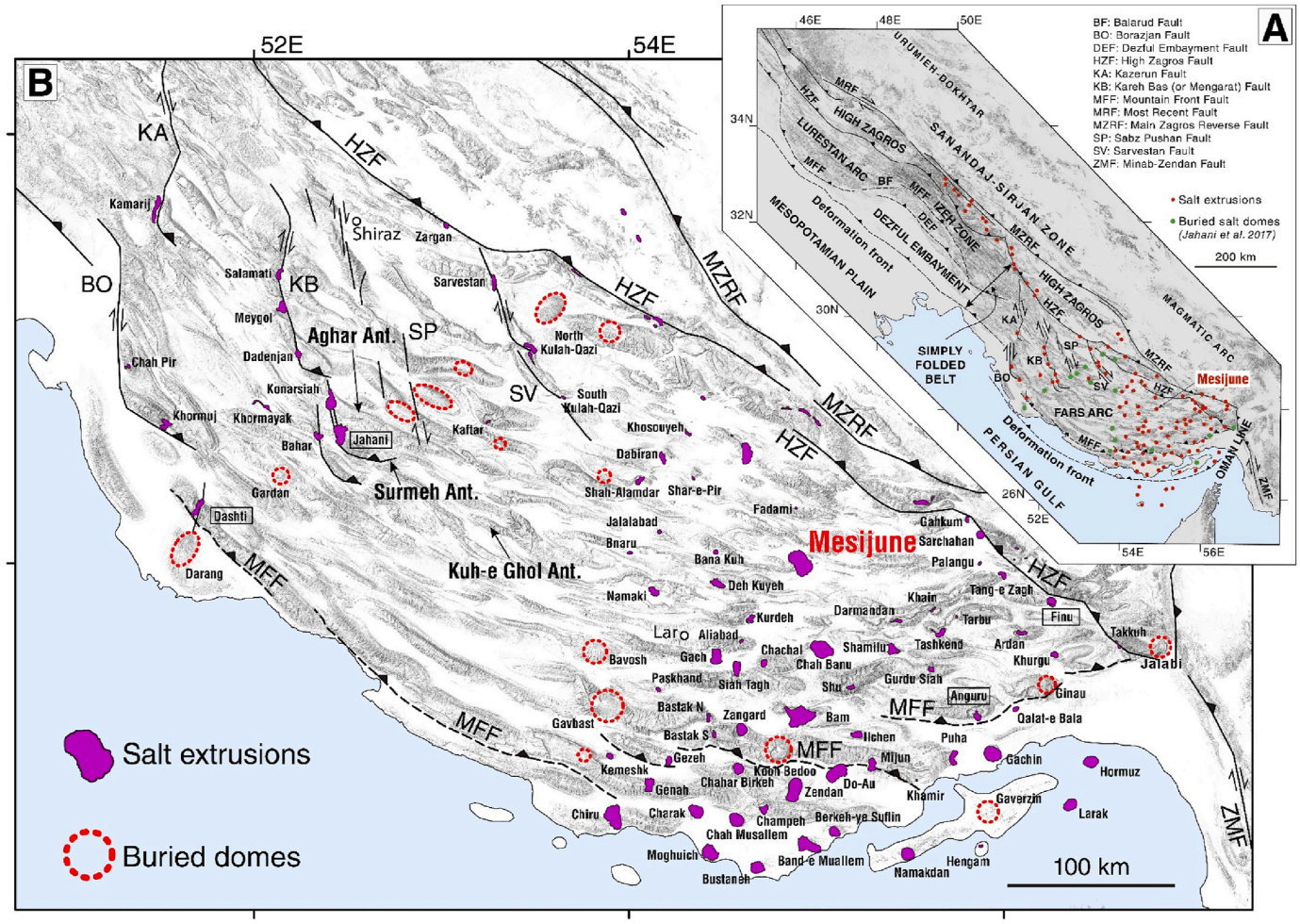


Fig. 1. Regional Geological Setting of the Zagros and Fars Arc indicating the location of the Mesijune salt diapir. A: Structural zonation of the Zagros Fold-and-Thrust Belt indicating the main faults and the distribution of salt extrusions and buried salt domes of the Neoproterozoic-Cambrian Hormuz Series. Buried domes based on Jahani et al. (2017). B: Hillshade of the Fars Arc showing the distribution of salt extrusions and buried domes. Note the apparent lack of salt diapirs in the central sector ascribed to an intra-basin structural high in the Hormuz Basin, known and the Qatar-Fars Arc. Mesijune in the southeastern Fars Arc is indicated with large bold letters. Salt extrusions mentioned in the text are marked with a rectangle.

both bounded by the High Zagros Fault (HZF in Fig. 1). The SE-propagating Zagros Deformation Front marks an ill-defined boundary between the Simply Folded Belt and the current foreland basin, associated with the Persian Gulf and the Mesopotamian Plain. The Simply Folded Belt is subdivided into three domains, including two arcuate segments separated by an intervening embayment, from NW to SE (Sepehr and Cosgrove, 2004): (1) the Lurestan Arc; (2) the Dezful Embayment; and (3) the Fars Arc, east of the N-S Kazerun-Borazjan right-lateral strike-slip fault system (Fig. 1A). These domains are distinguished by the influence on the orogenic deformation of distinctive stratigraphy, the inherited extensional structures predating the Zagros orogeny, and, more significantly, by the effectiveness and areal distribution of salt layers (particularly the Hormuz salt) as regional detachment horizons (Sepehr and Cosgrove, 2004). The Mesijune salt extrusion is located in the southeastern sector of the Fars Arc (Fig. 1B).

The Fars Arc is characterised by an arcuate array of folds, the orientation of which changes from the typical NW-SE Zagros grain in the western half of the arc, to E-W and ENE-WSW trends roughly perpendicular to the convergence direction, on the eastern half (Fig. 1B). The structural style in the Fars Arc is dominated by detachment folds largely decoupled from the basement along the Hormuz salt of Neoproterozoic-Cambrian age (Mouthereau et al., 2006; Jahani et al., 2009; Snidero et al., 2025). An original thickness of 1-1.5 km is estimated for this diapir-source unit (Talbot and Alavi, 1996), currently lying at a depth of 11-15 km (Jahani et al., 2009). The Kazerun-Borazjan fault system coincides with the western boundary of Hormuz salt diapirs and extrusions in the Simply Folded Belt (Kent, 1979; Berberian, 1995; Talbot and Alavi, 1996; Sepehr and Cosgrove, 2004, 2005) (Fig. 1B). This structure is widely interpreted as a supra-salt tear fault system, the development of which has been conditioned by underlying down-to-the-E normal faults in the basement that defined the western edge of the Hormuz salt basin (Jahani et al., 2017). Thicker salt on the downthrown side of these basement faults controlled (1) the development of precursor (i.e., pre-shortening): diapirs; (2) thinner and weaker supra-salt cover above the diapirs; and (3) greater propagation of the contractional deformation towards the foreland east of the basement faults above thick salt (i.e., lower basal friction), resulting in the development of S-propagating dextral tear faults (Jahani et al., 2017). The same interpretation has been proposed for other N- to NNW-trending strike-slip faults in the western Fars Arc, that also offset dextrally folds and display rows of salt extrusions with progressively more juvenile morphology appearance towards the south (e.g., Kareh Bas Fault; Hassanpour et al., 2018; Gutiérrez et al., 2024) (Fig. 1B).

The Fars Arc hosts more than one hundred Homuz salt diapirs typically associated with anticlinal ridges (Harrison, 1930; Kent, 1958, 1979, Bosák et al., 1998; Jahani et al., 2009; Gutiérrez et al., 2023a, 2023b) (Fig. 1B). A large proportion of the diapirs in the Zagros have emerged at the surface (passive diapirism) to form the most remarkable

suite of salt extrusions in a terrestrial environment worldwide. Others remain as buried diapirs, the inflated roofs of which are typically expressed as domal morpho-structures with crestal normal faults superimposed on the anticlines (active diapirs; Gutiérrez et al., 2023a, b). Salt diapirs in the Fars Arc are mainly distributed in two sectors (Fig. 1B): (1) the northwest limb, where the majority of the diapirs occur at transtensional zones associated with dextral supra-salt strike-slip faults (Talbot and Alavi, 1996; Gutiérrez et al., 2024, 2025a, 2025b); and (2) the eastern half, where diapirs are mostly associated with anticlines lacking any relationship with surface faults (Jahani et al., 2007; Snidero et al., 2019). The absence of diapirs in the intervening area is attributed to thin or absent Hormuz salt in an intra-basin horst, designated as the Qatar-Fars Arch (Jahani et al., 2017).

A great part of the diapirs were initiated long before the current

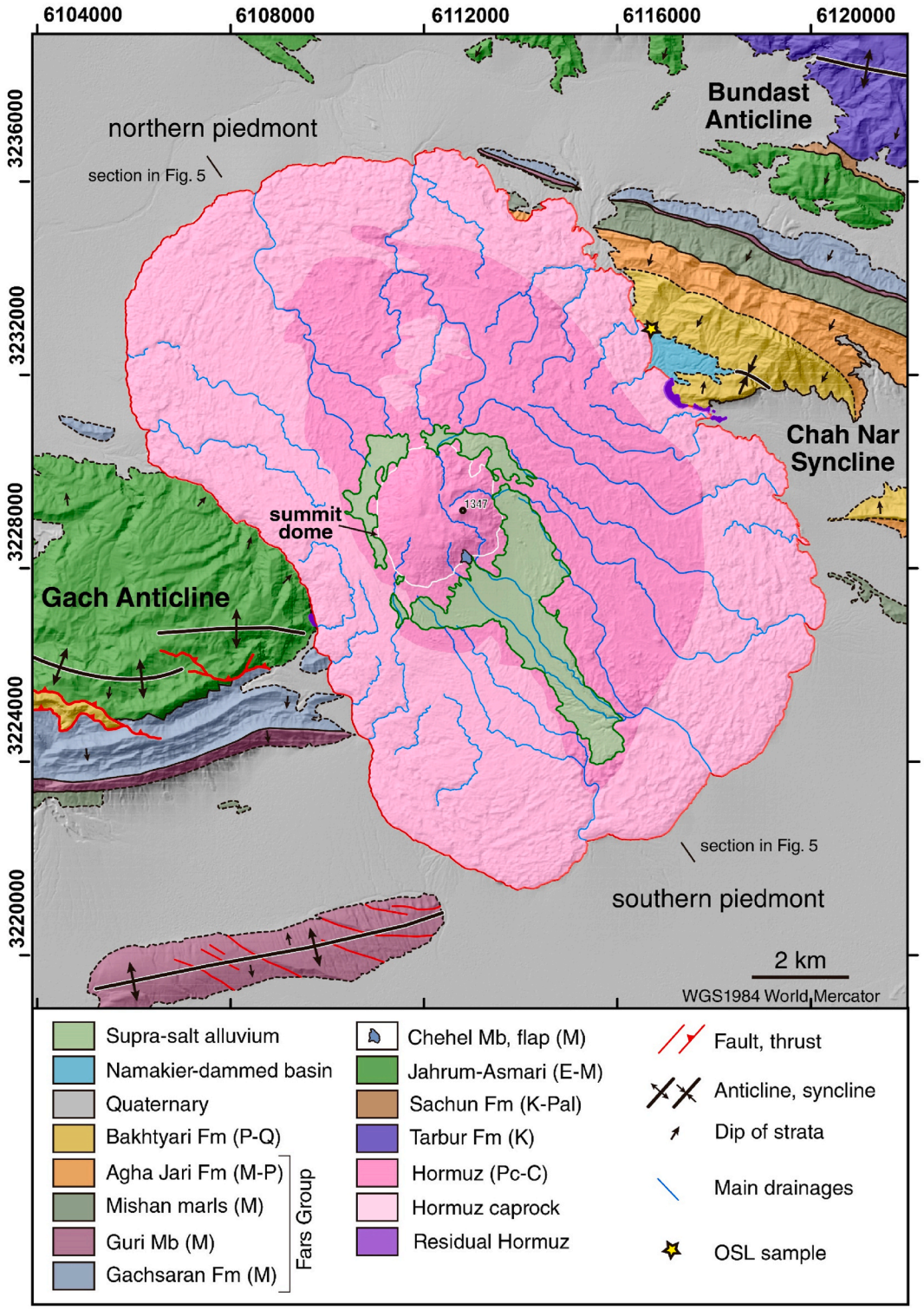


Fig. 2. Geological map of the Mesijune salt fountain and its surroundings. The map depicts the elongated supra-namakier basin develop atop the SE-directed salt sheet downslope of an obstructing bedrock inlier. It also depicts the marginal namakier-dammed basin. Location of OSL sample collected in the sediments of the latter basin indicated with a yellow star. (Pc:Precambrian; C: Cambrian; K: Cretaceous; Pal: Paleogene; E: Eocene; M: Miocene; P: Pliocene; Q: Quaternary).

orogenic stage, as revealed by stratigraphic and structural evidence in pre-shortening formations associated with the diapirs (Harrison, 1930; Kent, 1979; Jahani et al., 2007, 2009; Snidero et al., 2019, 2025). Passive and active diapirism during pre-orogenic times is recorded by (1) Hormuz-derived debris sourced from emerged diapirs; (2) thickness and facies variations, hiatuses, and growth strata in syn-kinematic sediments associated with the diapirs (i.e., halokinetic sequences) (see recent review in Jahani et al., 2007).). Their formation is interpreted as driven by basement extensional faulting combined with differential loading (Snidero et al., 2019, 2025). Most of these precursor diapirs were reactivated in the Cenozoic shortening, leading to their squeezing (Ezati Asl et al., 2019; Snidero et al., 2025). These mechanically weak bodies have also played an important role during the orogeny development as strain localizers and enhancers, that often controlled the initiation, propagation and geometry of folds and faults (e.g., deflections, bends, constrictions, stepovers) (Letouzey and Sherkati, 2004; Callot et al., 2007, 2012; Jahani et al., 2007, 2009, 2017; Snidero et al., 2019, 2025; Gutiérrez et al., 2024, 2025b).

The onset of the main contractional deformation in the Zagros foreland (Simply Folded Belt) is linked to the continental collision between the Arabian and Central Iranian microplates that occurred during deposition of a regressive succession overlying the laterally extensive Asmari Limestone of Oligocene-early Miocene age (Sepehr and Cosgrove, 2004). This late Cenozoic sequence comprises the early Miocene-Pliocene Fars Group (Gachsaran, Mishan and Agha Jari formations), and the unconformable conglomeratic Bakhtyari Formation (Plio-Quaternary) (Fig. 2). Growth strata, onlaps, and angular unconformities within the Fars Group record progressive propagation of the deformation towards the SW (Hessami et al., 2001). Consistently, the basal unconformity of the Bakhtyari conglomerates, which records the onset of significant morphogenetic folding and unroofing of anticlinal ridges (Mouthereau et al., 2007; Gutiérrez et al., 2023a, 2023b), is progressively younger towards the current foreland. This shifting of the deformation front suggests that the onset of diapir rejuvenation by contractional loading has migrated towards the foreland, and that a general chronological trend could be expected, with older salt extrusions towards proximal sectors of the orogenic wedge. Ruh et al. (2014), based on a magnetochronological investigation, dated the onset of fold growth (i.e., base of growth strata) in the Kuh-e Ghol Anticline at ca. 3.8 Ma during Agha Jari deposition (early Pliocene). This anticline is located around 160 km west of Mesijune diapir at a more distal trend (see location in Fig. 1B). Folding in the Mesijune area likely initiated prior the main deformational phase, potentially occurring during Gachsaran deposition. This is supported by its proximal position to the hinterland and the possible influence of a weak precursor diapir, which may have localized and accelerated early fold nucleation (Callot et al., 2007, 2012; Dooley et al., 2009). This timing is consistent with basal onlaps and growth strata in the Miocene Gachsaran Formation on the limbs of anticlines further west (Aghar and Surmeh anticlines; Fig. 1B), lying at a trend equivalent to that of Mesijune (Hessami et al., 2001).

3. Methodology

Preliminary geological and geomorphological mapping was carried using remote-sensed data and small-scale geological maps (Fig. 2). The initial maps were refined during a field campaign carried out in November 2023, using a tablet with georeferenced satellite images for navigating and locating observation and sampling points. The available geological maps covering the study area include 1:250,000 scale compilation maps (Perry et al., 1965; NIOC, 1977), and 1:100,000 scale geological sheets (Masibeygi, 1965; Noroozi, 1966; NIOC, 1977; Sedaghat et al., 2005). The remote-sensed data used include: (1) grey-scale aerial photographs from 1956 printed at an approximate scale of 1:45,000 and interpreted under a stereoscope; (2) Satellite images (Google Earth, ESRI World Imagery) with a resolution of 0.6-1 m; and (3) TanDEM-X DEMs (12 m resolution; German Aerospace Center, DLR) and derivative relief models. These DEMs, generated from bistatic X-Band interferometric Synthetic Aperture Radar (SAR) data acquired by the satellites TanDEM-X (TDX) and TerraSAR-X (TSX), which have absolute and relative vertical accuracies of <10 m and 2-4 cm, respectively (Wessel, 2016). The mapping process and the morphometric and spatial analyses were carried out with ArcGIS Pro, and using the TanDEM-X DEMs for 3D computations.

A sample (MESI-1) of fine-grained detrital deposits was collected for OSL dating (Optically Stimulated Luminescence) from a marginal namakier-dammed basin. The sample was collected in block form due to its high degree of cementation. The inner part of the block (not exposed to light) was extracted for equivalent dose (D_E) determination, while the outer portion was used for external dose rate (D) calculation (Table 1).

The extracted block sample was used for equivalent dose (D_E) analysis and external dose rate (D) calculation (Table 1). Luminescence measurements were carried out at the CENIEH Luminescence Dating Laboratory in Burgos, Spain, using a Risø TL/OSL DA20 reader, equipped with bialkali EMI 9235QB15 photomultiplier tubes and a 90SR/90Y beta source (dose rate of ~0.10 Gy/s). Blue light (470 nm) was used for stimulation. Quartz grains of sizes 180-250 μm were mounted on stainless steel discs and fixed using a 2 mm patch of silicone oil. Quartz multi-grain aliquots were measured following the Single-Aliquot Regenerative-dose (SAR) protocol (Murray and Wintle, 2000, 2003) to obtain representative dose distributions. Final D_E values were estimated following the Central Age Model (CAM; Galbraith et al., 1999; Duller, 2008). Environmental dose rates (D) were calculated as a contribution of beta, gamma and cosmic radiation, and were derived from radionuclide activity concentration determined by ICP-MS analysis and the following parameters: dose rate conversion factors (Guérin et al., 2011), alpha and beta grain size attenuation factors from Brennan et al. (1991) and Guérin et al. (2012), water content attenuation from Aitken and Xie (1990), and etching attenuation factors from Brennan (2003). Cosmic dose rate was calculated following Prescott and Hutton (1994) considering depth, altitude, longitude and latitude. A 5% error has been added to the estimated water content used for the correction. Environmental dose rates to an infinite matrix values have been calculated using the Dose Rate & Age Calculator (DRAC, Durcan et al., 2015). Additional details on the analytical protocols of the CENIEH Geochronological Laboratory can be found in del Val et al. (2022).

Surface changes were estimated from time-series analysis of the European Space Agency's (ESA) C-band SAR satellite Sentinel-1. Both

Table 1
Summary table of OSL dating results on quartz grains including sample codes, the calculated dose rates and the parameters used for computing dosimetry, the estimated equivalent dose (D_E), and the derived age expressed in kiloyears before present (ka). A 5% error has been added to the estimated water content. Error margins are presented at 1-sigma. n/N: Number of aliquots that passed SAR acceptance criteria/total measured aliquots. Number of aliquots presented in the abanico plot (Fig. S3); OD: Overdispersion; CAM: Central Age Model; D_E: Equivalent dose.

Field code	MESI-1
Lab code	LM23233-01
Coordinates	40R 298200E 3102449N
Water content (%)	5
Depth (m)	9.4
238U (ppm)	1.41 ± 0.04
232Th (ppm)	2.88 ± 0.10
87Rb (ppm)	22.1 ± 0.7
40K (%)	0.59 ± 0.01
Cosmic dose rate (Gy/ka)	0.08 ± 0.01
Dose rate (Gy/ka)	1.13 ± 0.05
Grain size (μm)	180-250
n/N	3/24 (19)
OD (%)	69
Age Model	CAM
DE (Gy)	16.2 ± 2.8
Age (ka)	14.3 ± 2.5

ascending (track 130) and descending (track 166) observations were processed using the Small Baseline Subset (SBAS) technique (Berardino et al., 2002). The ascending data includes 222 images acquired between 01.12.2014 and 29.06.2023, while the descending data includes 209 images collected between 29.02.2014 and 21.04.2023. For each track, a network of small temporal baseline interferograms was generated using the Alaska Satellite Facility's Hybrid Pluggable Processing Pipeline (HyP3) system (Hogenson et al., 2020). The Copernicus GLO-30 Public DEM (https://doi.org/10.5270/ESA-c5d3d65) was employed by the HyP3 system for topographic phase removal and geocoding during InSAR processing.

In total 972 and 800 interferograms were generated to form small baseline networks of interferograms with the ascending and descending track data, respectively. A multilooking factor of 2 in azimuth and 10 in range was applied to the interferograms. Before phase unwrapping, an adaptive filter with alpha = 0.6 was applied to the interferograms to reduce phase noise (Goldstein and Werner, 1998). The time series analysis was performed using the MintPy package (Yunjun et al., 2019). The network of interferograms was inverted using least squares to retrieve time series data (Berardino et al., 2002), and the topographic residual errors were estimated and subtracted from the time series (Fattahi and Amelung, 2013). A temporal coherence threshold of 0.9 was applied to mask out pixels with high noise level (Pepe and Lanari, 2006). The vertical and east-west deformation rates were estimated from the line-of-sight measurements in the two geometries neglecting the north component (Wright et al., 2004). The decomposition process considered sensor geometry, with an incidence angle of approximately 41° and a look angle azimuth of approximately 77° for ascending track, and an incidence angle of approximately 44° with a look angle azimuth of approximately 283° for descending track.

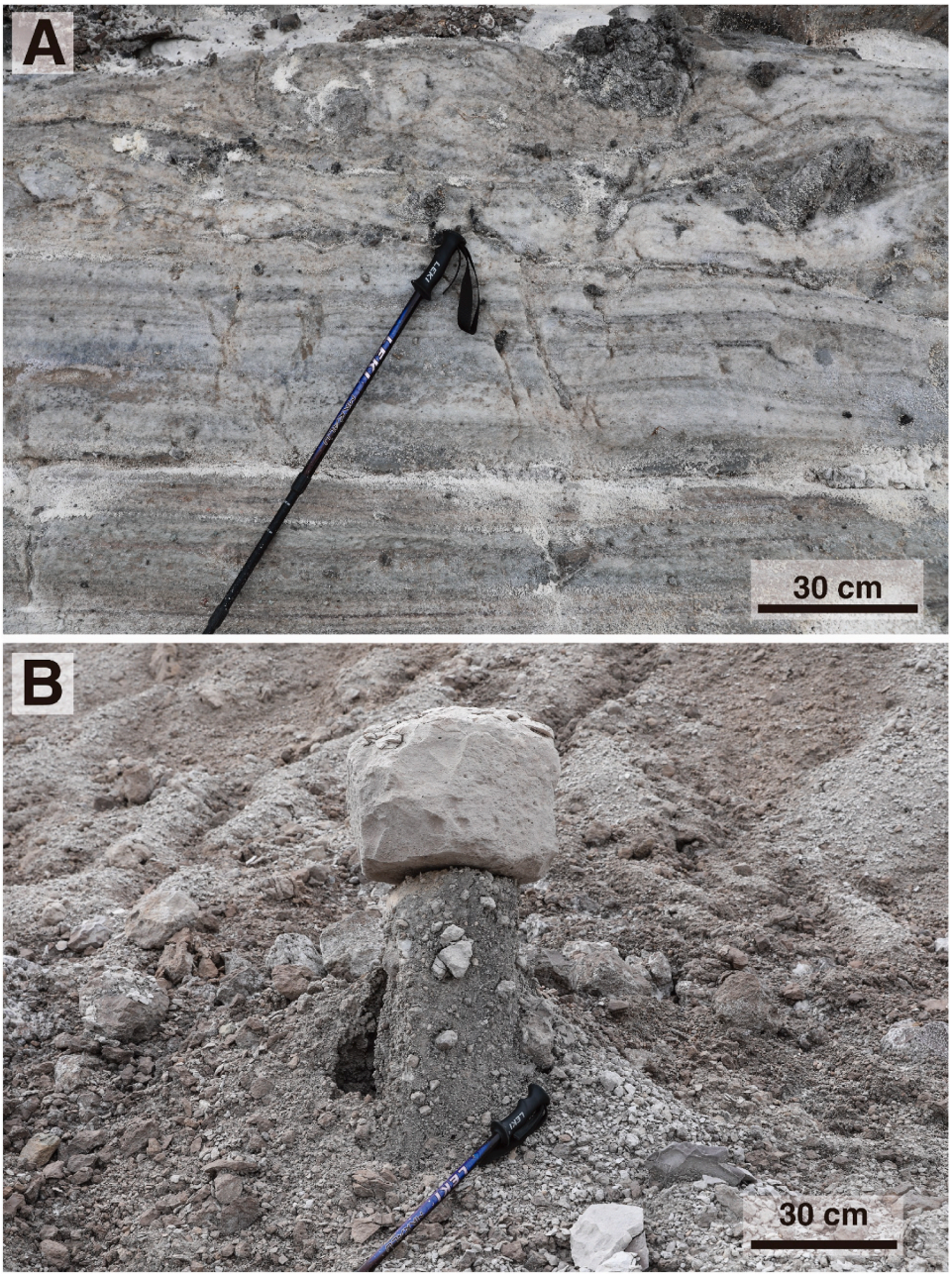


Fig. 3. Outcrops of the Hormuz salt in Mesijune diapir. A: White-grey bedded salt with floating, angular gravel-sized inclusions. B: Pedestal with a stem of massive dirty salt with a high proportion of angular granule-to cobble-sized inclusions.

4. Results

4.1. The geology associated with the mesijune salt extrusion

The following bedrock cartographic units have been differentiated in the geological map covering the Mesijune salt extrusion and its vicinity (Fig. 2): (1) Extruded Neoproterozoic-Cambrian age salt of the Hormuz Group. (2) The Late Cretaceous limestone of the Tarbur Formation. (3) The Late Cretaceous-Paleocene, marl-rich Sachun Formation. (4) A thick Eocene to Early Miocene limestone- and dolomite-dominated succession including the Jahrum and Asmari formations. (5) The Miocene, gypsum-rich Gachsaran Formation, which comprises three members undifferentiated in our map; gypsum of the lower Chehel Member, the limestone-rich and ridge-forming Champeh Mb., and marls and gypsum of the upper Mol Member. (6) The Miocene Mishan Formation, consisting of a basal limestone unit (Guri Member), overlain by a thick succession of greenish marls. (7) Marls and sandstones of the Mio-Pliocene Agha Jari Formation. (8) The unconformable continental conglomerates, sandstones and mudstones (molasse) of the Plio-Quaternary Bakhtyari Formation.

The limited outcrops of the Hormuz Group in the Mesijune salt extrusion indicate that it mainly consists of white-to-grey, banded-to-massive halite, with intercalations of anhydrite, variegated siltstones, and limestone. Locally, relatively thick black limestone packages are observed forming protruding ridges (Fig. 3A). Halite beds often include a high proportion of floating, angular granule-to boulder-sized inclusions of various lithologies, mainly multi-coloured siltstones, limestone, anhydrite, and green tuff (Bosák et al., 1998; Sedaghat et al., 2005) (Fig. 3B). These inclusions are likely derived to a great extent from brittle layers interbedded within the Hormuz Group. Diapiric flow of the salt, sourced at a depth of around 11-15 km, was accompanied by brecciation and comminution of the brittle layers, plus the dissemination of the derived clasts within the plastic salt mass. The exposures of Hormuz bedding in the namakiers typically show a dipping or folding structure, with a strike perpendicular to the downslope flow direction and dominant upflow dip of bedding and fold axes (i.e., downflow vergence of recumbent folds; Jackson and Hudec, 2017).

From a structural perspective, the Mesijune salt fountain is located between two ridge-forming WNW-ESE trending folds; the Gach Anticline to the SW and the Chah Nar Syncline to the NE (Fig. 2). The Gach Anticline is an asymmetric fold, which steeper southern limb is ruptured by S-verging reverse faults that offset Plio-Quaternary Bakhtyari conglomerates (Perry et al., 1965). The periclinal nose of this anticline occurs on the SW side of the salt fountain, where beds attain a fold-normal attitude. Jahani et al. (2009), in a geological cross-section across the Fars Arc located west of Mesijune, based on seismic images, unpublished geological maps, well information, and field data, depicts the Gach Anticline within a pop-up bounded by reverse faults in both limbs. The southern N-dipping fault offsets the whole supra-salt cover, while the northern one is shown as a secondary backthrust linked to the main S-verging fault. The development of these reverse faults is probably favoured by primary welding at the base of the overburden after long-sustained detachment folding and salt flow (e.g., Molinaro et al., 2005). The Chah Nar fold is a WNW-plunging asymmetric syncline with a steeper northern limb and Bakhtyari detrital sediments in the core (Fig. 2). Here, the Bakhtyari Formation shows an overall fining upward succession, controlling the development of an erosional depression in the younger units associated with the fold hinge. South of the Mesijune salt extrusion the Quaternary alluvium in the southern piedmont is interrupted by an inlier of Guri limestone that forms a small anticlinal ridge, probably related to a shallow parasitic fold detached along the Garchsaran Formation (Noroozi, 1966).

At the base of the SE flank of the summit dome, there is an outcrop of countryrock surrounded by Hormuz salt, that was reported by Bosák et al. (1998) as a facet of Miocene bedrock (Fig. 4). This cream-coloured inlier is a flatiron-shaped bedrock spur 250 m wide and 150 m in local relief encircled by the extruded salt. Its lithology, dominated by gypsum, suggests that it corresponds to the Chehel Member of the Miocene Gachsaran Formation (Fig. 2). Bedding is largely obscured by extensive gypcretes, but it can be observed on its flanks, where it shows a NE-SW strike concordant with the edge of the summit dome and steep SE dips (ca. 80°) or even overturned. The poor exposure conditions preclude elucidating if the upturning of the beds operated during deposition (e.g., growth strata), or whether it is entirely

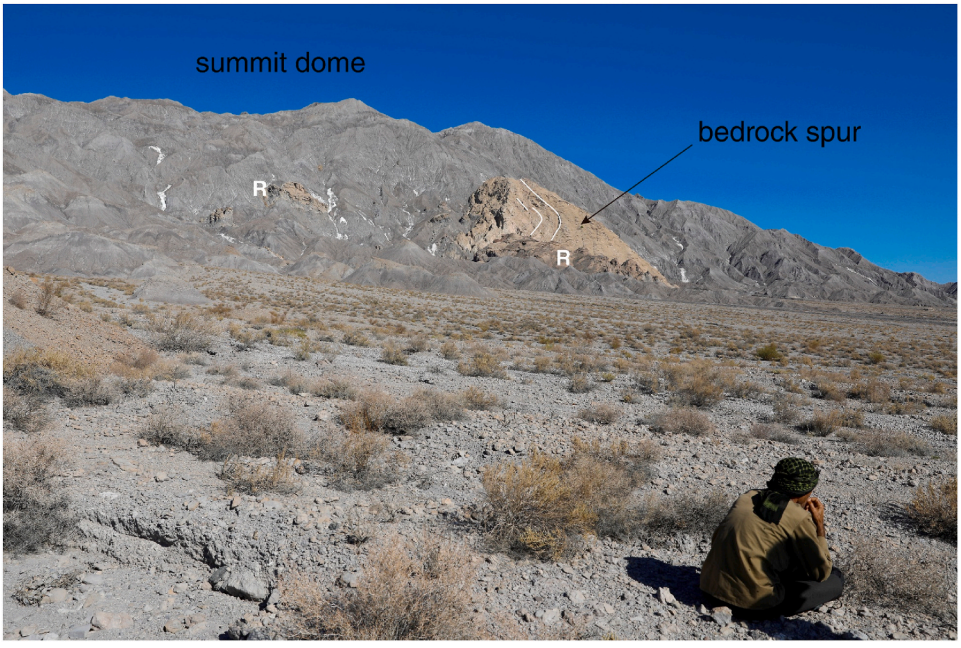


Fig. 4. Southern flank of the summit dome with an inlier of upturned strata (Chehel Member of the Gascharan Formation). This bedrock spur functions as a buttress for the salt in the summit dome and as an obstructing splitter for lateral flow in the southern namakier. Note badlands landscape in the steep salt slopes covered by a thin veneer of clay-rich dissolution residue. At the foot, proximal sector of alluvium-filled depression with active alluvial fans. R stands for thick and indurated dissolution residue.

postsedimentary. Some lines of evidence support the concept that the folded strata may correspond to a flap formed at the edge of a rising diapir during Gachsaran deposition: (1) the upturned strata seem to be disconnected from the folds flanking the salt fountain, being offset to the N with respect to the southern limb of Gach Anticline; (2) the NE-SW strike of the bedding is concordant with the edge of the summit dome and the underlying salt feeder, and does not conform with the transverse strike (ca. N-S) of the bedding in the pericline of the Gach Anticline; (3) studies on evidence of synorogenic sedimentation and magneto-chronological data suggest that folding and rejuvenation of precursor diapirs in Mesijune area likely started during deposition of the Gachsaran Formation (Hessami et al., 2001). Jahani et al. (2007), in a table and a map compiling data on the timing of activity in the diapirs of the Fars Arc, indicate for Mesijune: "late Miocene-Pliocene activity evidenced by thinning of strata and facies change". However, the name of the formations and the location where these relationships were observed are not indicated.

4.2. General features of the salt fountain

The Mesijune salt fountain has a surface area of 137 km^2 and a local relief of 650 m between the summit dome (1347 m a.s.l.) and the southern namakier front (Fig. 2). We have roughly estimated a volume of 11,650 Mm^3 for the salt extrusion considering: (1) the 3D space defined by its topography and a basal surface interpolated from its perimeter; and (2) a correction factor of 0.8 to account for the general drop of the base of the salt glaciers from the feeder to the front of the namakiers. This factor has been estimated from a longitudinal cross-section of the extrusion and the interpretation of the geometry of the salt base (i.e., proportion of salt above the interpolated basal surface) (Fig. 5). This volume, equivalent to a cube with a side of around 2.3 km, is 1.4 times larger than that estimated for the Jahani salt fountain in the western Fars Arc (Gutiérrez et al., 2025a) (Fig. 1B).

The summit dome, with a slightly eccentric position displaced to the SW, shows a circular perimeter expressed as a well-defined junction between the steep flanking slopes and the surrounding gently-sloping namakiers (Figs. 2, 4, and 5). This dynamic bulge above the salt feeder is 2.7 km across, covers 5.48 km^2 (4% of the salt fountain), and has a local relief of 230 m (35% of the total relief). The western half of the summit dome shows a relatively flat crest. In contrast, on the eastern half, the dome crest is deeply dissected by three major drainages with intervening sharp-crested salt ridges (Fig. 2). The steep slopes of the summit dome on its western flank and in the deeply entrenched eastern half display dense gully networks carved in recently expelled rock salt covered by a thin veneer of grey clayey dissolution residue (i.e., capsoil) (Figs. 2 and 4).

The extruded salt has spread radially from the summit dome towards lower ground to form a multidirectional salt sheet or namakier (Fig. 2). On the SW and NE sides salt flow has been constrained by ridges (Gach Anticline and Chah Nar Syncline, respectively), while it has spread unconfined to the NW and SE, prograding over piedmont alluvium. Thus, the salt sheet comprises two principal NW- and SE-directed lobes of similar length and the salt fountain has an overall elongated morphology; 16.3 km long, 8.6 km wide, elongation ratio 1.9. The salt fountain shows an asymmetric longitudinal topographic profile, with higher topography and thicker salt on the NW lobe, despite the southern piedmont lies at lower elevation (700 versus 770 m a.s.l. in the S and N piedmont, respectively) (Fig. 5). This asymmetry may be ascribed to lower salt supply on the SE side, where the flow is partially obstructed by the bedrock spur (Fig. 4). The transverse NE-SW profile is also markedly asymmetric, being the namakier on SW side considerably higher, thicker and steeper than on the NE side. This can be attributed to the shorter distance on the SW side between the summit dome and the anticlinal buttress, forcing the namakier to surmount the ridge and accumulate a larger volume of salt under compressional flow (Fig. 2). The overall slope of the NW, SE, NE and SW sides of the namakier, measured from the foot of the summit dome to the toe of salt glacier front, are, 3.3°, 3°, 3.1°, and 7.4°, respectively. In the bidirectional Jahani salt fountain, showing a juvenile morphological stage, the unconfined southern namakier that flows across a piedmont has an overall slope of 6.5°.

The proximal sector of the salt sheet, at the foot of the summit dome, displays an aureole of alluvial fan aprons fed by the drainage systems carved in the summit dome (Figs. 2 and 4). Here, the gravelly alluvium essentially consists of subangular clasts mostly derived from the non-soluble inclusions embedded in the Hormuz salt (Fig. 3), with a high proportion of siltstone and limestone. The development of these alluvial aprons is favoured by several factors (Gutiérrez et al., 2025a): (1) high runoff coefficient of the steep salt slopes underlain by low-permeability rock salt, favouring rapid dissolutional erosion and the release of large quantities of inclusions (Bruthans et al., 2008; Pérez-Villar et al., 2025, 2026); (2) the clasts are readily transported downslope; high slope gradient prevents the in situ accumulation of dissolution residues, especially gravel-sized particles; (3) prompt deposition at the foot of the summit dome, where the sharp slope attenuation involves an abrupt drop in flow competence (Blair and McPherson, 1994). Similar alluvial aprons have been documented at the foot of the summit dome of Jahani salt fountain. Here, some of those aprons have evolved into closed and semi-closed alluviated poljes with ponors (Gutiérrez et al., 2025a). The SE namakier displays a flow-parallel, elongated, alluvium-filled basin 4 km long and 800-900 m wide, described below.

In addition to the alluvial surfaces located along the periphery of the summit dome and on the SE namakier (7% of the salt extrusion), the salt fountain displays two other domains according to the surficial deposits and the associated landscape (Fig. 2). The summit dome and the proximal-medial sectors of the namakier are dominated by a badlands-like landscape of salt hills extensively covered by a thin, grey and slightly indurated clay-rich capsoil (Fig. 4). These areas represent 35% of the salt fountain. In the distal sector of the namakiers the salt is largely

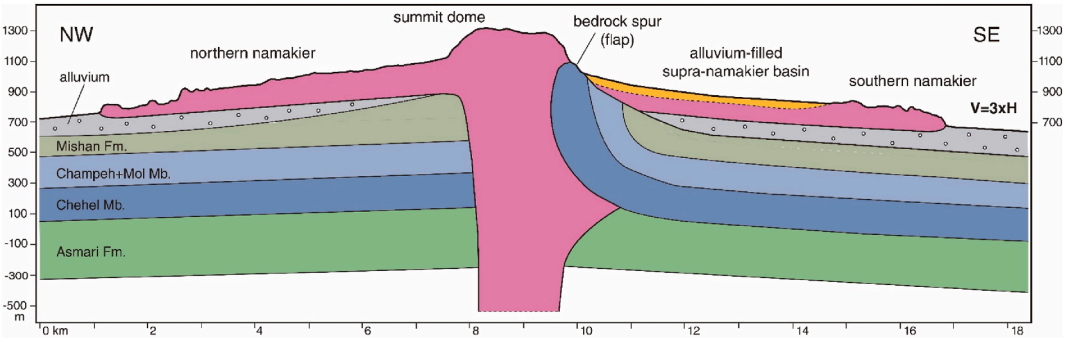


Fig. 5. Cross-section of the Mesijune salt fountain along its NW-SE major axis, depicting the bedrock spur on the SE flank of the summit dome as a flap and the alluvium-filled basin atop the SE salt glacier. Note higher topography in the NW namakier than in the SE namakier, where lateral salt flow is obstructed by the bedrock spur. Vertical exaggeration x3.

overlain by a thick and resistant caprock commonly consisting of cemented breccias with a light-coloured Ca-sulphate cement (anhydrite, gypsum) (Fig. 6). Caprock is the dominant cover, accounting for 58% of the salt fountain (Fig. 2). The caprock covers a proportionally much larger area on the narrower SE side of the namakier, and forms and isolated mesa-like outlier in the NE lobe. These caprocks, locally more than 20 m thick, are related to the long-sustained dissolution of Hormuz salt by the inward propagation of dissolution fronts, leading to the in situ accumulation of the insoluble components, accompanied by brecciation and cementation processes. The areas where the namakiers are covered by resistant caprocks display higher topography, lower degree of fluvial dissection, and numerous relatively large scarp-edged caprock collapse sinkholes (Fig. 7).

The namakiers display a general corrugated topography consisting of flow-normal ridges and troughs, being more conspicuous in the caprock than in the capsoil areas. These features can be attributed to a fabric in the bedrock related to the development of folds with flow-normal axes (i.e., downflow-verging recumbent folds), which have controlled differential dissolutional and mechanical erosion processes. In the SE namakier, this topographic fabrics of crescentic ridges reveals two lobes on both sides of the alluvium-filled trough, related to salt flow separation at the bedrock spur (Fig. 2).

Numerous salt extrusions in the Fars Arc show morphological and stratigraphic evidence of retreat, including trimlines on bedrock, and patches of in situ residual Homuz disconnected from the current salt extrusion, often forming moraine-like features (e.g., Gutiérrez et al., 2025a). Most of the peripheral area on Mesijune salt fountain lacks such features, indicating that its perimeter essentially delineates its maximum extent. However, on the NE flank of the extrusion, there is a peripheral band around 1 km long with remnants of residual Hormuz situated beyond the current namakier front (Figs. 2 and 7). These deposits perched on Bakhtyari conglomerates and resting piedmont alluvium attest that the salt fountain once reached a larger extent in this sector.

4.3. The supra-namakier basin

The SE namakier lobe displays an elongated alluvium-filled basin 4 km long and 800-900 m wide. The basin is oriented parallel to the flow direction and located downstream of the bedrock spur (Figs. 2 and 8). On both flanks of the basin, the namakier displays independent crescentic corrugations, revealing a composite salt lobe comprising two sublobes (Fig. 2). The distal termination of the basin is framed by higher ground ascribable to the frontal compressional bulge of the namakier underlain by resistant caprock. The proximal, non-dissected sector of the basin is dominated by active alluvial fans with a distributary braided channel system that turns into a contributory pattern in a downstream narrowing. In the medial and distal sector, the basin is deeply entrenched by steep-sided valleys carved into cemented alluvium (Fig. 9). The top surface in this sector mostly corresponds to a relict mantled pediment. This gently sloping surface is underlain by a deposit of cemented gravels a few meters thick with a planar erosional base. The surface of the pediment displays clasts coated by a brown desert varnish. This apparently non-deformed pediment cover overlies unconformably a thick alluvial fill of crudely-bedded cemented gravels with a persistent upstream dip of 10-15° (Fig. 9). The elevation difference between the top of this alluvial unit in areas where it has not been bevelled by the pediment (south-easternmost sector) and the floor of the entrenched valleys indicate a minimum alluvium thickness of 50 m.

4.4. The namakier-dammed marginal basin

On the NE margin of the salt fountain there is namakier-dammed basin associated with an erosional depression, carved in Bakhtyari sediments along the core of the WNW-ESE oriented and WNW-plunging Chah Nar Syncline (Figs. 2, 10, and 11). The basin shows an orientation parallel to the fold axis and displays a westward-widening triangular shape, 1.8 km long along the medial axis, and covering 97 ha (Fig. 11). The depression, currently externally drained, contains a lacustrine-palustrine fill of well-bedded and well-sorted fine-grained facies, unconformably overlain by gravels of a mantled pediment (Fig. 12). The pediment surface and the associated gravelly cover shows a general slope converging towards the axis of the basin and its northern outlet. The pediment deposits exhibit markedly different lithological composition related to the contrasting provenance (Figs. 10 and 11). On the NE side of the basin, mainly derived from outcrops of the Bakhtyari Formation, they mainly consist of poorly sorted gravel and display a light brown colour, whereas those on the opposite side, derived from the Hormuz namakier, display a dark grey colour and have abundant gypsiferous cement. The sector where the marginal basin was dammed



Fig. 6. Supra-salt caprock consisting of chaotic packbreccia and floatbreccia embedded in a white Ca-sulphate (gypsum, anhydrite) cement.



Fig. 7. Northeastern flank of the SE-directed salt glacier showing evidence of retreat, including a veneer of residual Hormuz on a slope underlain by Bakhtyari, and disconnected masses of Hormuz located beyond the current front of the glacier. Arrow points to an inclusion of Hormuz stranded on the Bakhtyari slope.

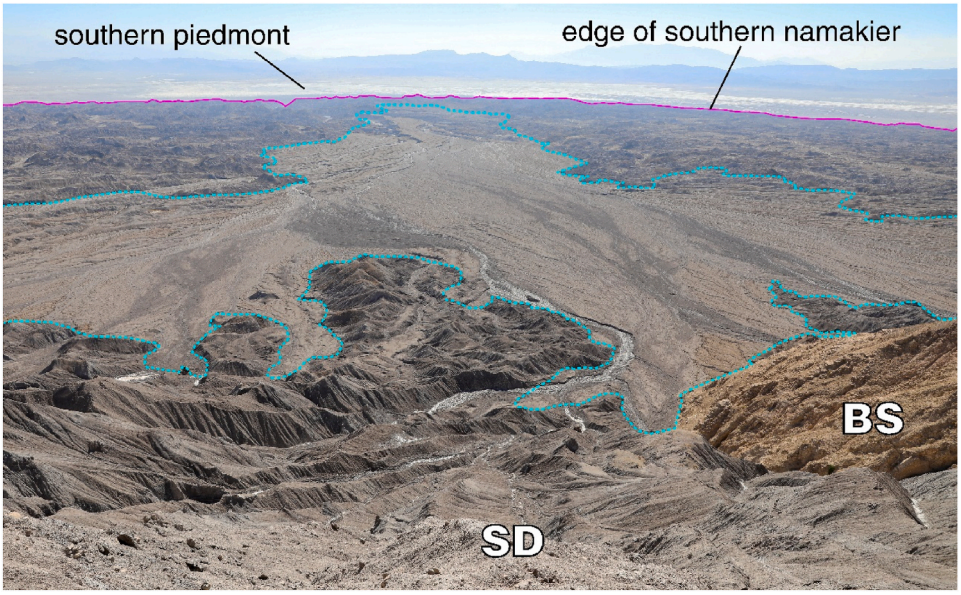


Fig. 8. View of the southern namakier from the summit dome (SD) with a longitudinal alluvium-filled depression in front of the bedrock spur (BS) of upturned strata of the Miocene-age Chehel Member. The depression, surrounded by higher ground, was once an enclosed expanding basin lying atop a southward spreading salt sheet.

by the namakier is expressed as Hormuz sediments overriding hills of Bakhtyari conglomerates. Here, the NW-directed stream that currently drains the basin has carved a straight and narrow canyon through Bakhtyari conglomerates (stream section depicted with dashed line in Fig. 11).

A sample was collected from the lacustrine basin fill for OSL dating close to the outlet of the basin (Fig. 12). Here, fluvial dissection has exposed a 5.2 m thick succession of lacustrine-palustrine deposits, consisting of tabular beds of clayey sands and silts with scattered granules and some lenticular beds of subrounded granule-pebble gravel. This unit is overlain by pediment gravels 5.5 m thick with a discordant erosional base related to the syndepositional dip of the alluvium. The sample of cohesive silt, extracted 1.3 m above the base of the exposure and 3.9 m below the erosional top of the unit, has yielded an OSL age of 14.3 ± 2.5 ka. Unfortunately, the sample yielded poor luminescence results because of two factors: (1) the amount of quartz in the deposit, chiefly derived from the carbonate-dominated Bakhtyari Formation, was very low (<0.20 g) and insufficient to measure over 24 aliquots; and (2) only 3 out of 24 measured aliquots met acceptance criteria (Figs. S3 and S4). However, the equivalent dose calculation is not affected, whether calculated using the full distribution (n = 19) or only the three discs (Fig. S3). Therefore, this geochronological result should be considered with caution. Dose recovery preheat test results, OSL decay curves and dose response curves, abanico plot of D_E distribution and SAR acceptance criteria plots are presented in Figs. S1, S2, S3, and S4 of Supplementary data.

4.5. DInSAR kinematics of the salt fountain

The spatial and temporal patterns of surface displacement in the Mesijune salt fountain are characterised with DInSAR models of vertical and horizontal (E-W) velocity, together with LOS displacement time series. Note that the displacement captured by the DInSAR approach may be the net result of several processes, mainly including salt flow, erosion (dissolutional and mechanical), and subsidence related to subsurface dissolution. Different fundamental modes of salt flow may operate, including vertical rise, vertical fall (e.g., Vendeville and Jackson, 1992; Dooley et al., 2009), and lateral spreading-gliding that may be accompanied by uplift and subsidence related to compressional (i.e., thickening) and extensional (i.e., thinning) flow.

The vertical displacement rate model shown in Fig. 13A displays a consistent pattern with the main geomorphic domains of the salt fountain, although with some asymmetry. Displacement in the summit dome, unresolved in the previous works (Barnhart and Lohman, 2012; Shami et al., 2024), is dominated by negative velocity values as low as -41 mm/yr, indicating greater lowering in the northern sector. In

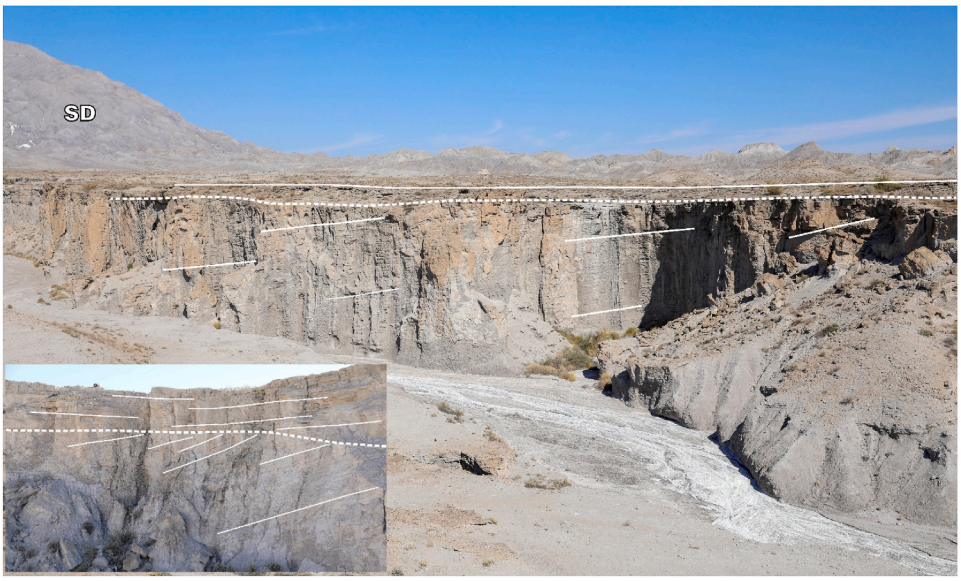


Fig. 9. Deeply incised alluvium-filled depression atop the southern namakier. The exposure shows two units of alluvial deposits bounded by an angular unconformity. The deformed strata in the thick lower unit dip upstream, whereas the upper mantled pediment deposit shows a syndepositional downstream dip concordant with the aggradation surface. Inset image shows a closer view of the unconformity exposed in a different drainage. SD stands for summit dome.

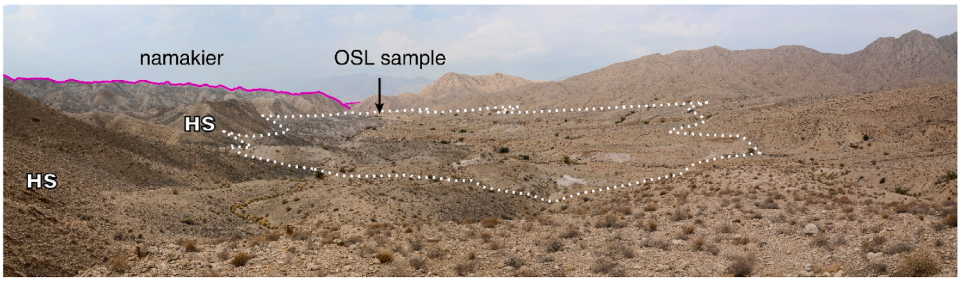


Fig. 10. Namakier-dammed basin on the NE flank of the salt extrusion filled with paleolake deposits covered by mantled pediments. OSL sampling site indicated. HS stands for Hormuz series.

contrast, in a portion of the southern sector associated with the bedrock spur, the dome crest exhibits uplift with positive rate values that reach 5 mm/yr. The NW namakier shows subsidence in the proximal sector from around -10 mm/yr that decreases gradually to negligible or null values in the distal sector. The SE namakier is dominated by null to very low positive vertical displacement rate values (<5 mm/yr). Relatively lower values around 0 mm/yr occur along a longitudinal NW-SE oriented band that coincides with the alluvium-filled supra-namakier basin underlain by thinner salt. Spatially restricted subsidence areas (-3 to -7 mm/yr; labelled as S in Fig. 13A) occur associated with clusters of caprock collapse sinkholes with evidence of activity (i.e., fresh concentric fissures and scarps). The combined NW-SE topographic and vertical displacement rate profiles shown in Fig. 13B reveal a clear longitudinal asymmetry in the morphology and kinematics of the salt fountain attributable to the buttressing-obstructing effect of the bedrock spur located on the SE flank of the summit dome. The transverse SW-NE topographic and vertical displacement rate profiles depicted in Fig. 13C illustrate the larger length and lower thickness of the salt glacier on the NE flank of the salt fountain determined by the greater distance between the feeding vent and confining ridge. Slightly higher uplift (2-3 mm/yr) is observed on the SW sector of the namakier, ascribable to compressional flow related to the frontal buttress. This velocity profile also shows how the sense of vertical displacement in the summit dome varies depending on the proximity to the bedrock buttress. The average of the vertical displacement rates in the salt fountain (137 km^2; ca. 45 m pixel resolution) have a very low positive value of 0.8 mm/yr, suggesting an apparent net annual volume gain of 109,600 m^3. The mean of the vertical velocity values in the summit dome (5.48 km^2) is -16 mm/yr, yielding a net yearly volume loss of -87,680 m^3.

Fig. 14A shows a model of horizontal displacement rate in the E-W direction. Note that this direction is oblique to the NW-SE elongation of the salt fountain that reflects the orientation of the main salt lobes. The model shows a good agreement with the distribution of the main geomorphic domains. Maximum eastward and westward displacement rates in the eastern and western sectors of the summit dome reach 144 mm/yr and 102 mm/yr, respectively. The namakiers display a progressive decrease in the horizontal displacement rate away from the summit dome up to null or very low values in the distal sector. The graph of Fig. 14B represents an E-W topographic profile alongside horizontal displacement rate in the E-W direction using the absolute values. These graphs illustrate the following features: (1) null or very low horizontal displacement in the central/crestal zone of the summit dome; (2) maximum lateral displacement in the laterally unconfined flanks of the summit dome; (3) higher lateral displacement in the eastern flank of the summit dome with greater local relief and degree of unconfinement (the western namakier is shorter, thicker and displays a convex longitudinal profile); (4) progressive attenuation of the lateral movement in the namakiers, from 20 to 30 mm/yr in the proximal sector to essentially stable glacier fronts.

The LOS displacement time series at specific points have been compared with monthly rainfall recorded at the Mazayjen-Zarindast meteorological station (20 km WNW of Mesijune) over a decade

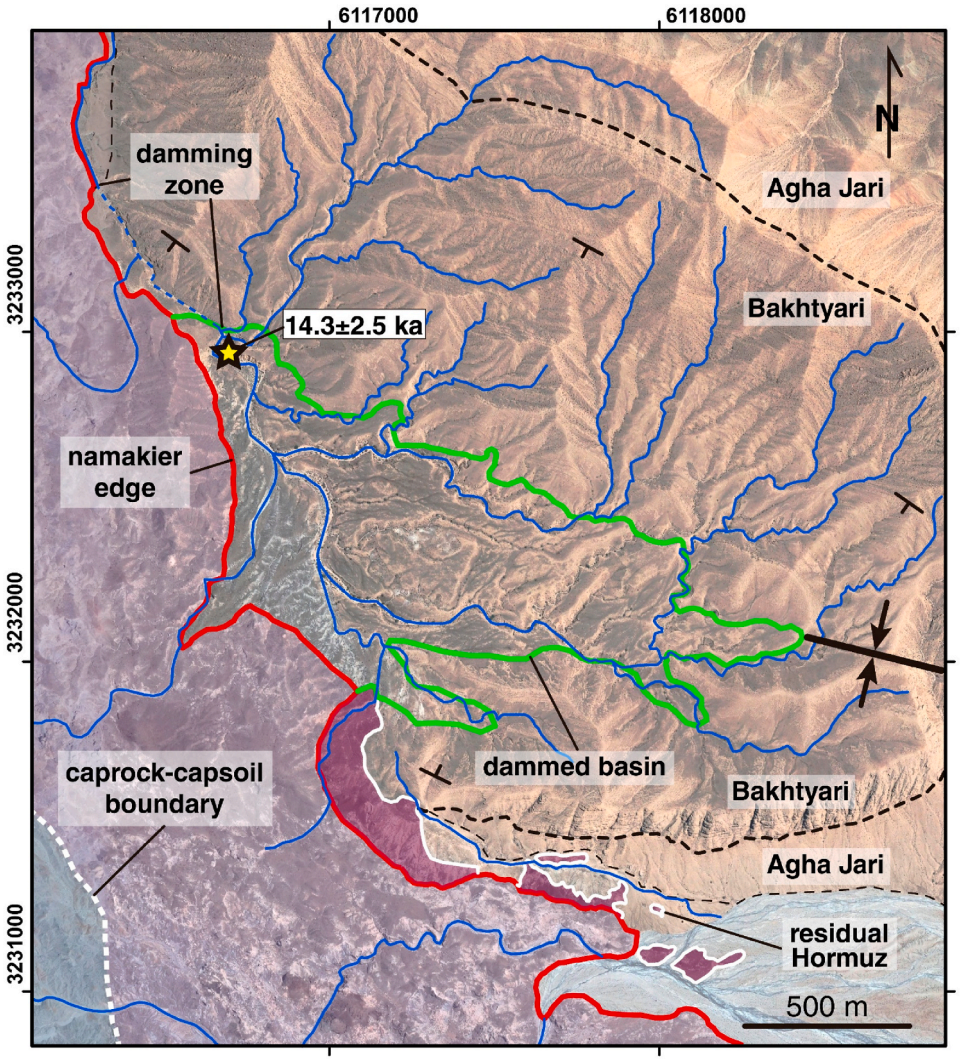


Fig. 11. Sketch of the namakier-dammed basin depicted on a satellite image downloaded from Google Earth (February 2024; Airbus satellite image; https://www.google.com/earth/). The map shows the distribution of residual Hormuz (purple polygon) recording greater local advance of the salt glacier. The location of the OSL sample collected from paleolake deposits is indicated with a yellow star.

(2015-2025), in order to unravel the kinematic style of salt flow and potential relationships with the rainfall regime. Five points have been selected, labelled in Figs. 13A and 14A: U: rising crest of summit dome; D: crest of summit dome subject to topographic lowering; F: steep western flank of the summit dome; and W and E: proximal sector of the namakier west and east of the summit dome, respectively. Point R on limestone outcrops at Gach Anticline was selected as a stable reference site (lat = 27.980°, long = 54.871°). Fig. 15 shows two graphs for each point: (1) LOS displacement time series from ascending (red) and descending (green) data; and (2) monthly rainfall, alongside residuals of the LOS displacement computed by removing the best-fit trend of the ascending (red) and descending (green) data, represented as discrete values and smoothed 2-month moving average. Overall, the graphs indicate continuous creep displacement at steady rates and no clear temporal correlation between the LOS displacement residuals (within the range ±2 cm) and the rainfall peaks (correlation coefficient <±0.1).

5. Discussion

5.1. The supra-namakier basin

The cartographic relationships and the architecture of the alluvium-filled basin indicates that it corresponds to a supra-namakier basin developed in a trough associated with a zone of limited salt supply downstream of the obstructing bedrock spur (Figs. 2, 4, 8, and 9). The basin, lying over an autosuture related to the coalescence of two salt lobes, experienced expansion by the downslope translation of its distal edge, as the composite salt sheet advanced across the piedmont. This peculiar basin kinematics, with a quasi-stationary sedimentation locus within a downslope translating basin, results in a basin fill with a general offlap arrangement, with progressively younger deposits in the upslope direction (Fig. 9).

Fig. 16 shows an evolutionary model for the supra-namakier basin. In an initial stage, the salt extrusion was expressed as a growing salt dome buttressed by the bedrock spur on the SE flank (Fig. 16A). When the dome reached a critical height for which the extrusion was unable to withstand its own weight, the extrusion started to spread towards the piedmont (juvenile salt fountain stage), forming two salt lobes separated by the bedrock spur, which functioned as a flow divider (Fig. 16B). Eventually, the flanks of the advancing and expanding lobes encircled the bedrock spur and merged to form an autosure with an associated supra-salt basin. The enclosed depression trapped alluvium derived from the dissolutional erosion of the summit dome (Fig. 16C). Dooley et al. (2012) differentiates between allosutures and autosutures, depending on whether they form between lobes sourced from different, or the same feeder. According to these authors, autosutures can form by overriding,

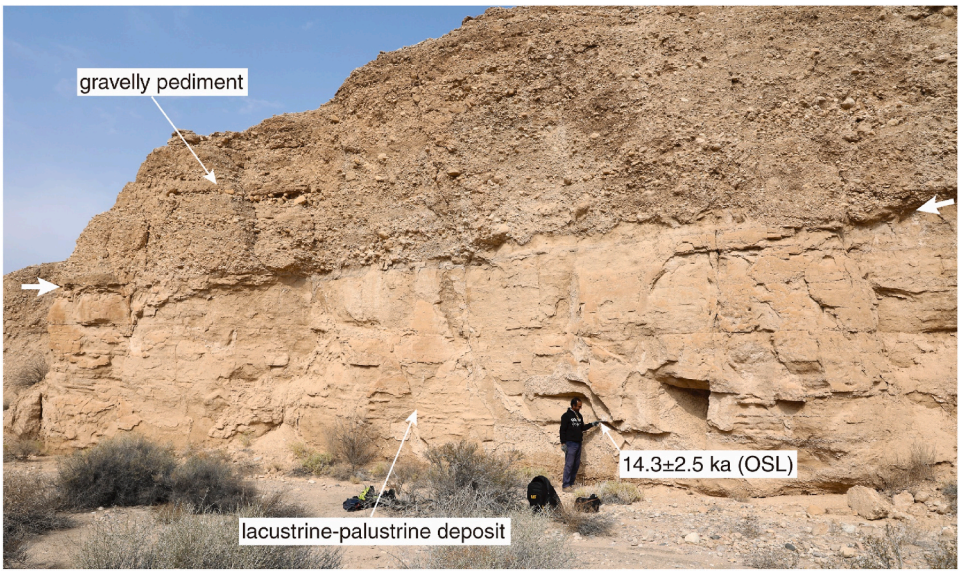


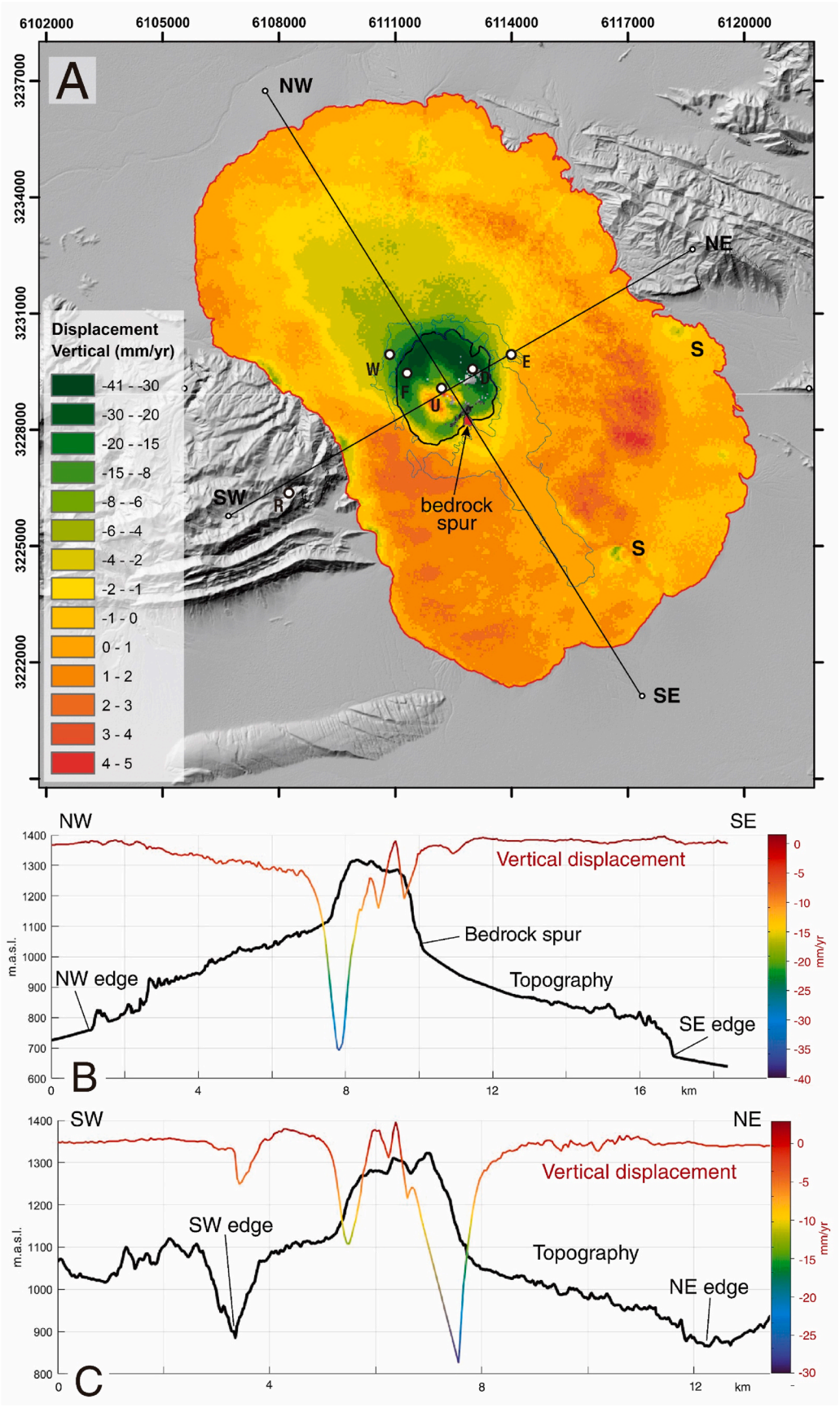
Fig. 12. OSL sample site. The exposure shows horizontally lying well-bedded fine-grained lacustrine-palustrine deposits unconformably overlain by gravelly mantled pediment deposits accumulated after the opening of the basin. Arrows mark unconformable contact. Location of sampling site indicated in Figs. 2, 10, and 12.

when the rear of a salt lobe advances over the front, or encircling, when a salt sheet diverges to bypass an obstacle and rejoins downstream. Following Dooley's et al. (2012) nomenclature, the studied supra-namakier basin has been developed in a trough associated with an encircling autosuture, where salt flow was limited by an obstacle. The spreading of the composite namakier across the piedmont was accompanied by the downslope translation of the distal edge of the basin and its lengthening. This fact explains the strongly elongated morphology of the basin (length/width ratio 4.4). The upslope dip of the exposed alluvium indicates that the basin has also experienced backward rotation at least in the distal and medial sector as supported by Fig. 9. This backtilting can be related to synkinematic differential thickness changes in the underlying salt, including compressional thickening in the frontal bulge and/or extensional thinning in its trailing zone. This mechanism may be favoured by the fact that as a multidirectional salt fountain expands, the flow is distributed across a progressively larger perimeter, resulting in an extensional flow (i.e., vertical contraction) upslope of the frontal bulge. Subsidence related to suballuvial salt dissolution does not seem to play any significant role, since this mechanism is expected to produce uneven and complex deformation patterns (e.g., multiple sagging basins, collapse structures bounded by normal ring faults) (De Waele and Gutiérrez, 2022) (Fig. 16D–F). The morphological degradation of the salt fountain by fluvial erosion (mature salt fountain stage) led to the capture of the enclosed basin by the drainage network (Fig. 16E). Following the capture, the medial and distal sector of the basin changed into a dominantly erosional regime. Firstly, a mantled pediment was developed cut across the backtilted basin fill during a period of relatively stable base level. Secondly, deeply entrenched valleys were carved by headward propagating streams into the basin fill. In contrast, the proximal sector of the basin remains essentially as a non-dissected aggradational zone in agreement with Fig. 8.

Secondary minibasins developed on allochthonous salt, both in marine and terrestrial environments, have been widely documented in the literature (Hudec and Jackson, 2006; Hudec et al., 2009; Kergaravat et al., 2016; Jackson and Hudec, 2017; Canova et al., 2025a). However, the analysed basin, although developed on moving allochthonous salt, does not meet the key attributes of minibasins. Minibasins are depressions surrounded and underlain by salt (or salt welds) filled by sediments with growth stratal geometries, which fundamental subsidence mechanism is the expulsion of salt from beneath and its rise around the basin margins (Jackson and Hudec, 2017). These sinking salt-expulsion basins can translate downslope atop laterally flowing salt sheets, rotate, become grounded against infra-salt rocks, and be encased or encapsulated by salt (e.g., Canova et al., 2025a). Some authors have proposed classifications for minibasins based on different criteria. According to their position with respect to the associated diapirs, Simmons (1992) differentiates interdomal, interlobal, and supralobal minibasins. Smith (2004) categorised them according to their cartographic shape into silled, partially silled, and tortuous. The shallow basin reported in Mesijune salt fountain, clearly not negatively buoyant, cannot be described as a minibasin, since its formation is not related to salt expulsion from beneath. Instead, it could be described as a supra-manakier basin, that was initially interlobal and became supralobal as the salt lobes merged, and as a silled basin (internally drained) that transformed into an open basin after its capture. To our knowledge, this is the first time a supra-namakier basin of this kind is documented in the literature. Further research may lead to the discovery of similar examples in both marine and terrestrial environments.

5.2. *The marginal namakier-dammed basin*

The cartographic and stratigraphic relationships, together with the limited geochronological data, allow the reconstruction of the following evolution for the namakier-dammed marginal basin developed at the NE edge of the salt fountain (Figs. 2 and 10–12). The spreading of the namakier eventually overwhelmed the erosional capability of the NW-directed trunk stream that used to drain the syncline-centred depression carved by in Bakhtyari sediments (Fig. 11). The namakier buried the original salt-margin valley associated at the Hormuz-Bakhtiary contact, creating an internally drained depression upstream. This event, occurred sometime within or before 14.3 ± 2.5 ka, formed an internally drained lacustrine-palustrine basin with rather continuous deposition of fine-grained deposits (Fig. 12). The obstructing effect of the topographic ridge created a local compressional wave in the namakier, resulting in salt built up (i.e., inflation) and greater spreading in nearby zones, as suggest the disconnected masses of residual Hormuz mapped to the south of the basin (Figs. 2, 7, and 11). At some stage, likely after 14.3 ± 2.5 ka, the basin was opened through the excavation of a straight canyon in resistant Bakhtyari conglomerates (drainage section depicted with dashed line in Fig. 11). Under this exorheic conditions, firstly, a mantled pediment was developed, which erosional base cut across progressively older deposits towards the axis and outlet of the



(caption on next page)

Fig. 13. Decomposed vertical displacement data. A: Vertical displacement rate model. B, C: NW-SE and NE-SW topographic profiles (TanDEM-X DEM) alongside vertical deformation rate profiles covering the summit dome and the radially spreading namakier. The location of the bedrock spur on the SE flank of the summit dome is indicated. S stands for subsidence areas associated with clusters of active caprock collapse sinkholes. Note asymmetric patterns of displacement controlled by external (anticlinal ridge on the SW) and internal (bedrock spur) features with buttressing-obstructing effect. Dots with letters indicate the points for which displacement time series have been plotted in Fig. 15.

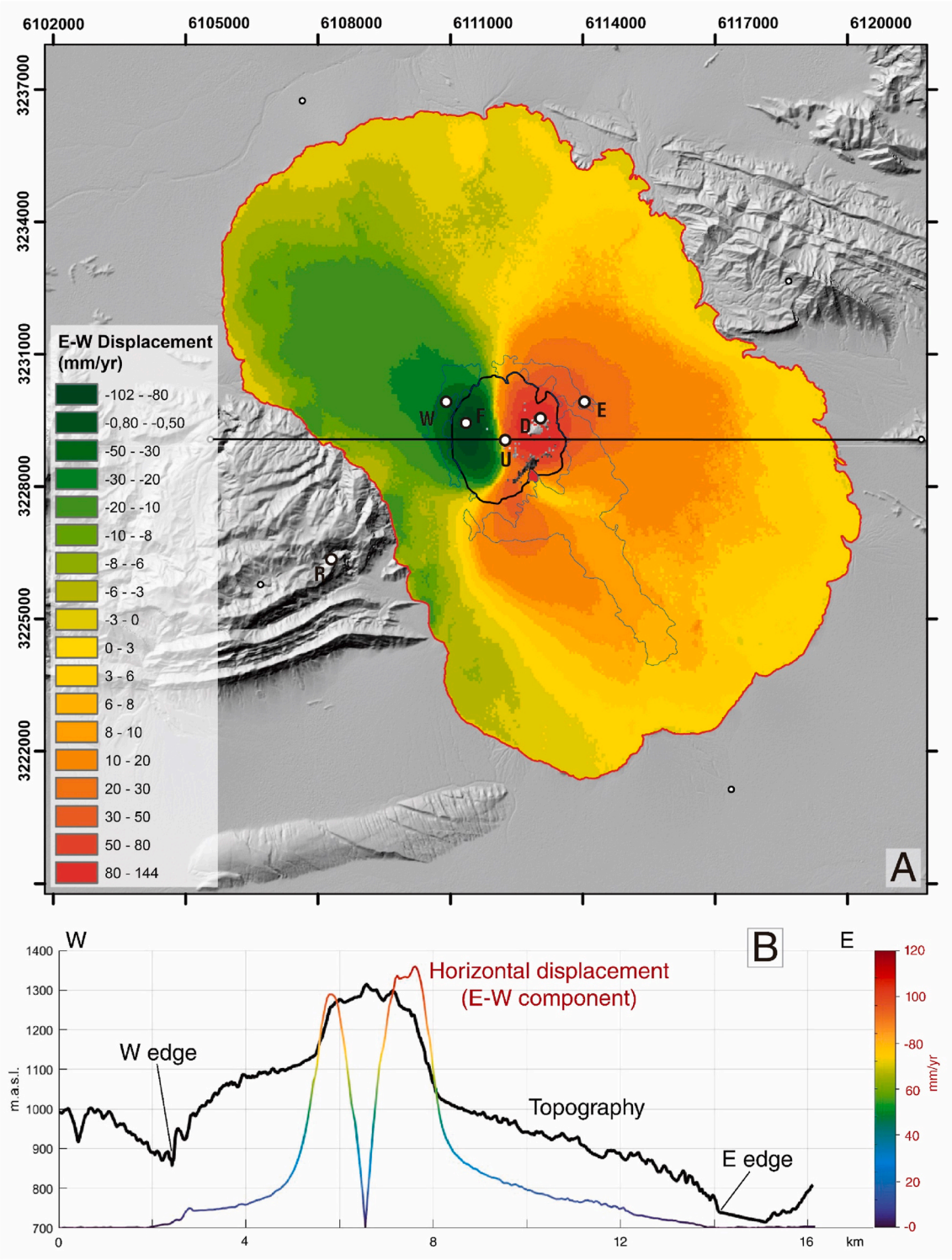


Fig. 14. Decomposed horizontal (E-W) displacement data. A: Horizontal displacement rate model. B: E-W topographic profile (TanDEM-X DEM) alongside E-W horizontal displacement rate profile (absolute values). Dots with letters indicate the points for which displacement time series have been plotted in Fig. 15.

basin (Fig. 12). This pedimentation phase was followed by the current fluvial dissection stage expressed by the entrenched drainage system.

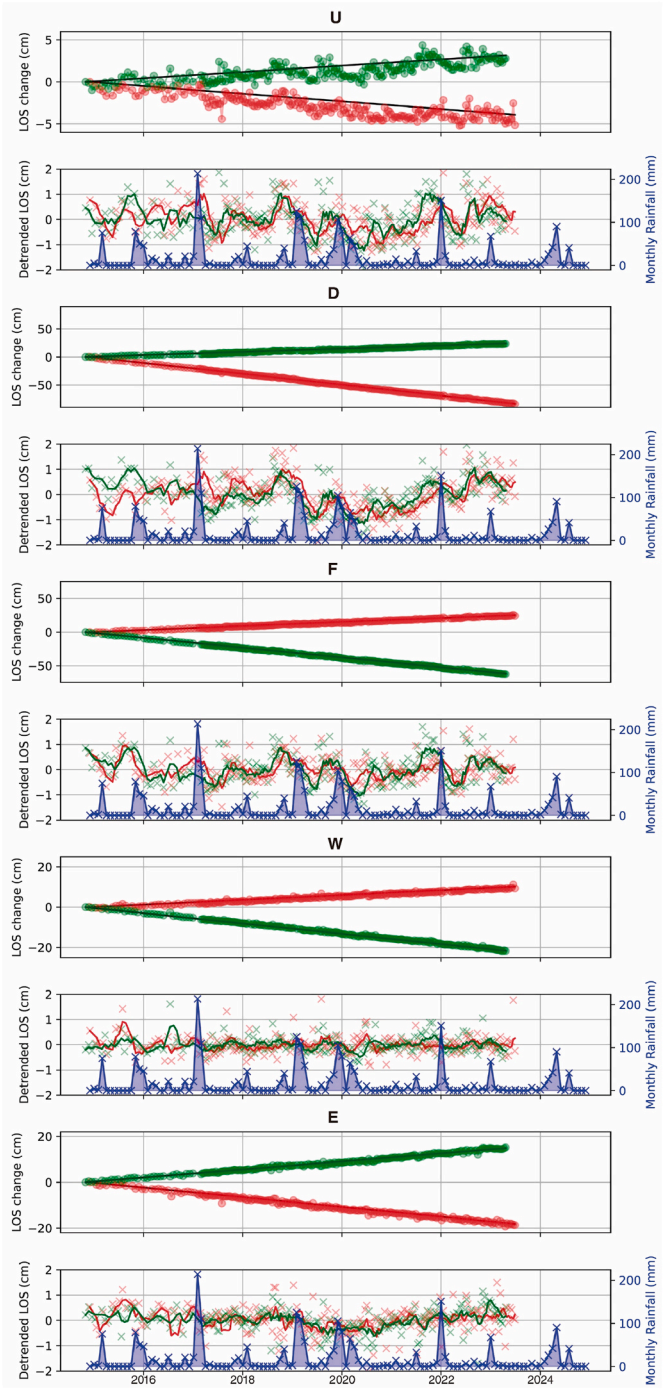


Fig. 15. Graphs showing temporal variation of LOS displacement from ascending (red) and descending (green) data at five points (U, D, F, W, E; labelled in Figs. 13 and 14). For each point, the upper graph depicts the LOS displacement time series and the lower graph monthly rainfall data from Mazayjen-Zarindast (20 km apart) and residuals of the LOS displacement after removing the best-fit trend, plotted as discrete values and 2-month moving average. Positive LOS values indicate displacement toward the satellite, while negative LOS values represent displacement away from the satellite.

Gutiérrez et al. (2025b) documented the damming of a major river by a namakier of the Jahani salt extrusion at around 28 ka, leading to the creation of a large paleolake upstream. In this case study, the obstruction of the namakier was also accompanied by local expansion of the salt fountain, recorded by disconnected masses of residual Hormuz.

The damming of the marginal basin by Mesijune namakier occurred during the deglacial transition from the LGM (Last Glacial Maximum) to the early Holocene, characterised worldwide by abrupt, millennial-scale fluctuations (e.g., Clark et al., 2012). The OSL age obtained from the paleolake deposits is centred within the Bolling-Allerod (14.7-12.9 ka), which according to several records (lake sediments, loess, stalagmites) was a period of relatively warmer and more humid conditions in the Zagros (Soleimani et al., 2023 and references therein). Nonetheless, the chronology of the damming event is not well-constrained, and paleoclimate variability probably did not play a decisive role. Other factors, such as the timing at which the salt fountain approached the confining ridge, or the variable erosional effectiveness of the local drainage related to erratic storms may have governed both the damming and dam-breaching processes.

5.3. *Present-day kinematics*

Several studies address the kinematics of salt fountains in the Fars Arc of the Zagros Mountains using DInSAR data, including Finu (or Syahoo; Aftabi et al., 2010; Zebari et al., 2025), Anguru (Ghassemi and Roustaei, 2021), Dashti (or Kuh e Namak; Zhang and Alves, 2024), Jahani (Gutiérrez et al., 2025b) and Mesijune (or Shah-Gheyb; Barnhart and Lohman, 2012; Shami et al., 2024) (names of these extrusions marked with a polygon in Fig. 1B). Anguru, Dashti and Jahani display laterally confined unidirectional or bidirectional namakiers that flow from anticlinal ridges towards the adjacent piedmonts. In contrast, Finu and Mesijune have multidirectional namakiers reflecting radial spreading of salt sheets from the summit dome. Finu, Anguru, Dashti and Jahani are salt fountains at a juvenile stage, dominated by a polygonal karst landscape (i.e., densely packed sinkholes) and internal drainage (e.g., Abirifard et al., 2017; Gutiérrez et al., 2025a). In contrast, Mesijune salt fountain displays a mature evolutionary stage evidenced by numerous signs of morphological degradation related to dissolutional and mechanical erosion processes, including (Gutiérrez et al., 2026) (Fig. 2): (1) extensive caprocks tens of meters thick (ca. 58% of the area); (2) very limited salt outcrops; (3) predominance of fluvial landscapes over karst and fluviokarst landscapes; (4) dissected summit dome; and (5) a large share of the externally drained area (ca. 65% of the area). Only the DInSAR studies carried out in Finu (Zebari et al., 2025), Jahani (Gutiérrez et al., 2025a) and Mesijune (Shami et al., 2024) present decomposed vertical and horizontal (E-W) displacement data.

Barnhart and Lohman (2012) obtained orogen-wide LOS displacement time series using Envisat ASAR C-band data (2003-2010; ascending and descending orbits; ca. 150 m resolution) to identify active salt extrusions in the Fars Arc with a detection threshold of 3 mm/yr. This work presents limited results for the Mesijune salt fountain lacking information for the summit dome due to coherence loss. The displacement models show LOS displacement rates indicating radial spreading and values of around 20 mm/yr in the proximal sector of the namakiers. Shami et al. (2024) selected the Mesijune salt fountain as a test site to assess the performance of machine learning (ML) methods for predicting surface displacement in an active salt extrusion. Displacement time series (LOS, vertical, E-W) were computed using Sentinel-1 SAR data from the periods 2016-2019 and 2020-2022, and applying the New Small Baseline Subset (NSBAS) DInSAR technique. The 2016-2019 displacement data, together with 14 spatial data layers of different variables (topography, hydrology, remote sensing parameters, geology) were used to predict vertical and horizontal cumulative displacements through machine learning approaches. A total of 29 displacement models were developed considering each variable separately and several groups of variables. The prediction capability of models was assessed quantitatively and independently using the 2020-2022 displacement data. The evaluation revealed thattopographic variables are the ones with higher prognostic utility, and predictions of horizontal displacement are better than those for vertical. The DInSAR displacement rate maps provide data for the namakiers, but lack information in the summit dome. In agreement with our data, the horizontal (E-W) displacement rate reaches a

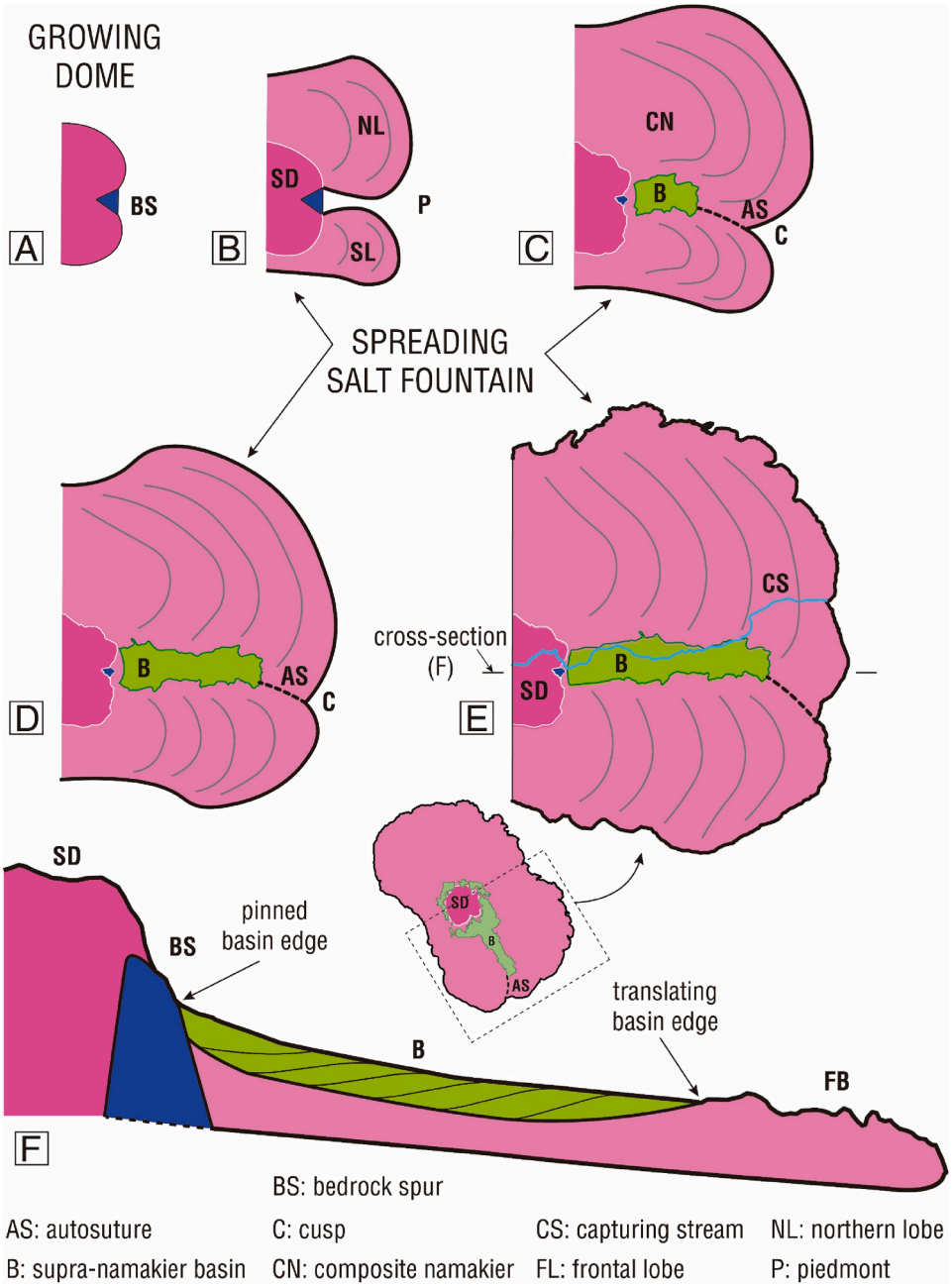


Fig. 16. Reconstruction of the evolution of the supra-namakier basin (A to E) and idealized longitudinal cross-section (F) of the salt fountain along the basin (not to scale). Inset above the cross-section is a plan view map indicating the portion of the salt fountain shown in E.

maximum value of 39 mm/yr in the proximal sector of the salt glaciers and decreases to nearly 0 at the front. Vertical displacements range between -18 mm/yr and 6 mm/yr and show predominance of subsidence in the NW salt lobe, while values are mostly around 0 in the SE lobe. Time series of LOS displacement at selected points in the namakier show a continuous ground movement at relatively constant rate. Nonetheless, spatial-temporal patterns of displacement are not comprehensively resolved (missing data in the summit dome) and the underlying mechanisms and controlling factors are not explained, largely because the main aim of the study was to assess the performance of ML.

This work presents for the first time decomposed DInSAR data for a multidirectional salt fountain at a degraded morphological stage, covering both the summit dome and the radiating salt sheets. Additionally, displacement patterns are explained in light of a sound geological-geomorphological characterisation of the salt extrusion and its vicinity based on field and cartographic data. In agreement with the mature morphological stage of Mesijune salt fountain, our vertical displacement data indicates that the summit dome is dominated by deflation, with lowering rates as high as -41 mm/yr. Uplift with a maximum velocity of 5 mm/yr occurs in a spatially restricted area associated with the bedrock spur, which acts as a buttress, preventing both lateral spreading and vertical contraction. Ghassemi and Roustaei (2021) report at the summit dome of the juvenile Anguru salt fountain maximum LOS displacement rates of 20-30 mm/yr, ascribable to both uplift and horizontal centrifugal flow away from the crest. In the crest of the summit dome of the juvenile Finu salt fountain, decomposed vertical displacement indicates maximum uplift values of 18 mm/yr (Zebari et al., 2025). The crestal zone of the summit dome of the juvenile Jahani salt fountain shows a dual pattern, with rapid subsidence (-100 mm/yr) on the northern sector associated with an erosional

escarpment 400 m high carved by a river, and uplift (10-20 mm/yr) in the southern sector, away from the debuttressing effect of the escarpment (Gutiérrez et al., 2025b). The integration of our vertical displacement rates in the summit dome yields an average surface lowering of -16 mm/yr and a net annual volume loss of 87,680 m^3. This value indicates that erosion, both dissolutional and mechanical, exceeds diapiric salt rise. Mechanical erosion most likely plays a significant role in this summit dome dissected by deeply entrenched gully networks. Considering that the 230 m high summit dome has a volume of 419,041, 910 m^3 and assuming a constant annual volume loss of 87,680 m^3, it could vanish in around 4779 years. A net annual volume gain of 109, 000 m^3 has been estimated for the whole salt fountain of Mesijune, considering an average positive vertical displacement rate of 0.8 mm/yr. These figures, taking into account the error margin of the values, essentially indicate a volume budget close to 0. In contrast, in the juvenile Finu salt fountain (17.98 km^2), Zebari et al. (2025) estimate an annual volume gain of 38.3 10^3 m^3/yr in the salt fountain, equivalent to an average positive vertical displacement rate of 2.13 mm/yr, almost three times higher than in Mesijune.

The highest E-W horizontal displacement rates occur on the laterally unconfined steep flanks of the summit dome. Horizontal displacement is higher on the eastern flank (up to 144 mm/yr) than in the western flank with lower local relief (up to 102 mm/yr). This asymmetric pattern is indirectly controlled by the surrounding topography and the distance to obstructing reliefs, which determines a shorter and thicker namakier in the SW side of the salt fountain. In the flanks of the summit dome of the Finu salt fountain, Zebari et al. (2025) document horizontal displacement rates of 60-70 mm/yr. Horizontal displacement rates in the steep flanks of the summit dome of Jahani associated with a non-truncated namakier reach values of 80-100 mm/yr (Gutiérrez et al., 2025b). Zhang et al. (2021) indicate maximum LOS displacement rates of 300 mm/yr and 62 mm/yr for the NE and SW flanks of summit dome of Kuh-e-Namak, without resolving the displacement components. The displacement pattern in the namakier surrounding the summit dome of Mesijune is consistent with its multidirectional spreading, where flow experiences divergence and attenuation as the perimeter increases. In agreement with Barnhart and Lohman (2012) and Shami et al. (2024), horizontal displacement rates show the highest values (20-30 mm/yr) in the proximal sector of the namakier and decrease to essentially null values at the distal edge, suggesting stasis in the position of the glacier front.

Vertical displacement shows apparent asymmetry in the namakier, with prevalence of subsidence in the NW lobe ($\geq$-10 mm/yr) and dominant uplift or null values ($\leq$5 mm/yr) in the SE lobe. Since the north displacement component is neglected in the 2D decomposition, any displacement in that direction is mainly incorporated into the estimated vertical component, with a minor effect on the east-west component. For the viewing geometries of the SAR data used in this study, 10 mm/yr of uplift would project to about 8 mm/yr and 7 mm/yr in ascending and descending LOS, respectively. A southward motion of roughly 50 mm/yr would produce a very similar LOS signal in both tracks (~7 mm/yr in ascending and ~8 mm/yr in descending). The same holds for subsidence and northward motion. As a result, the north and vertical components are not independently resolvable and neglecting the north component biases the estimated vertical displacement. Such a pattern can be observed in the estimated vertical displacement in the namakier, with prevalent estimated subsidence in the NW lobe (≥ -10 mm/yr) and dominant estimated uplift or near-zero values ($\leq$5 mm/yr) in the SE lobe. This pattern could not be explained based on geological-geomorphological evidence. It is therefore likely that a significant portion of the signal reflects non-modelled north–south deformation. Interpreted as leakage from non-modelled north motion, the apparent signal in the NW lobe would correspond to northward displacement on the order of 50 mm/yr, whereas in the SE lobe it would correspond to southward motion of ~25 mm/yr. This would be consistent with the multidirectional spreading, where flow experiences divergence and attenuation as the perimeter increases.

LOS displacement time series indicate, over a period of around one decade, continuous creep deformation at essentially constant rates and no relationship with the monthly rainfall data (Fig. 15). This kinematic style aligns with DInSAR data published for other salt fountains in the Zagros such as Finu (Zebari et al., 2025) and Jahani (Gutiérrez et al., 2025b) and challenges the conception whereby salt flow in the extrusions is dominated by an episodic displacement regime, governed by rainfall events that weaken the weathered outer zone that acts as a resistant carapace during dry periods (Talbot and Rogers, 1980; Talbot and Pohjola, 2009).

5.4. *Integration of long- and short-term data and practical implications*

The Mesijune diapir is located relatively close to the back edge of the Simply Folded Belt; around 25 km SE of the High Zagros Fault and 175 km NW of the current deformation front (Fig. 1B). The inception of the folds (Gach Anticline, Chah Nar Syncline) associated with a precursor Mesijune diapir and its rejuvenation by contractional loading likely occurred in the Miocene during Gachsaran deposition (Hessami et al., 2001). Probably, at this stage, salt inflation controlled sedimentation (e.g., thickness and facies changes; Jahani et al., 2007) and induced synsedimentary folding in the deposits situated atop and around a rising buried dome (i.e., halokinetic sequences). The upturned sediments of the Chehel Member of the Gachsaran Formation exposed on the SE flank of the summit dome are probably a flap developed during these early stages. This bedrock spur has acted as a buttress and an obstacle during the extrusive phase of the diapir, playing an important role in the development and kinematics of the salt fountain. Geometrical and cartographic relationships suggest that the extrusion of Mesijune diapir was initiated in the Quaternary after deposition of the Plio-Quaternary Bakhtyari conglomeratic formation. This stratigraphic unit, once deposited in a structural low, has experienced significant folding and relief inversion at Chah Nar synclinal ridge. The namakier of Mesijune is superimposed on this ridge, which has confined its advance on the NE flank.

As described above, during the extrusive stage, Mesijune diapir has evolved from a growing salt dome to a salt fountain with a supra-namakier basin associated with an encircling autosuture controlled by the obstructing bedrock spur (Dooley et al., 2012) (Fig. 15). Geochronological analyses (e.g., OSL) of samples collected from the oldest alluvium exposed in the supra-namakier basin would provide a minimum age for the basin development and the onset of the juvenile salt fountain. In the Late Pleistocene, the advancing namakier blocked a drainage system carved in the Chah Nar synclinal ridge, creating a namakier-dammed basin with lacustrine-palustrine deposition. At some stage, degradation processes started to prevail over salt rise and spreading, determining the transition of the salt fountain from a juvenile to a mature and degraded morphological stage. This change is probably related to a reduction in the expelling rate of the salt through the feeder, ascribable to depletion in the nearby source and/or secondary welding in the feeder. Main evidence for the degradation of the salt fountain include the predominance of fluvial landscapes and externally drained areas over the dominant polygonal karst landscape and internal drainage displayed by salt fountains at a juvenile stage (e.g., Zarei and Raeisi, 2010; Zarei et al., 2012; Gutiérrez et al., 2025a, 2026). DinSAR displacement data indicate that the summit dome is currently dominated by surface lowering, and that it could vanish in around 5 kyr, involving the transition of the salt fountain into a salt droplet. The frontal edge of the namakier is currently stable. Progressive degradation of the salt glacier by weathering and erosion (dissolutional and mechanical) ultimately will result in a sheet around 130 km^2 in area of residual Hormuz showing a selective preservation of coarse grained breccias. This stratigraphic evidence of past salt sheet advance has been documented in other salt extrusions of the Zagros (Jahani et al., 2007; Gutiérrez et al., 2025b) and in the geological record worldwide (e.g., Cofrade et al.,

2023).

The investigated salt fountain illustrates that salt sheets developed in terrestrial environments are expected to have lower potential and performance as reservoir seals and safe geostorage sites than those formed in marine settings because of the following features. First, terrestrial salt sheets tend to have lower areal extent and thickness due to slower spreading rates and more rapid degradation by weathering and erosion. Dissolution is widely regarded as the main process responsible for the degradation of salt sheets in subaerial environments. However, the Mesijune salt fountain shows that fluvial erosion can prevail over dissolution in mature salt sheets (e.g., Gutiérrez et al., 2026). Second, terrestrial salt sheets are expected to have poorer sealing capacity related, not only to their lower thickness and extent, but also to the greater presence of permeability zones through which fluids can leak. Potential fluid migration pathways can be related to the following features: (1) thin salt zones related to sheet advance across irregular topography; (2) thick caprocks developed at the top of the sheets; (2) relatively deep karstification in the salt below the caprock, potentially favoured by deep intrasalt base levels related to fluvial incision (e.g. Bruthans et al., 2024); and (3) autosutures of significant lateral extent, which may be associated with supra-namakier basins filled with highly porous deposits.

6. Conclusions

The Mesijune salt fountain records a protracted history of active and passive diapirsm within a contractional setting, involving several stages: (1) rejuvenation of a precursor buried diapir, likely since Miocene times; (2) salt breakout and extrusion leading to a growing salt dome; (3) lateral salt spreading to form an expanding juvenile salt fountain dominated by karst landscapes and internal drainage; (4) at present, prevalence of degradation processes over salt expelling, expressed as a mature salt fountain dominated by fluvial landscape transitioning into a salt droplet.

The past and current dynamics of the salt extrusion has been significantly influenced by bedrock obstacles located within the salt fountain and along its periphery. A bedrock spur situated on the flank of the summit dome acted as a flow divider, determining the development of two salt lobes that eventually merged to form an encircling autosuture with an associated supra-namakier basin. The bedrock spur controls the current displacement pattern in the summit dome, dominated by vertical lowering, except in the vicinity of the spur, where its buttressing effect prevents lateral spreading and favours local uplift. The external ridges located on the NE and SW flanks of the salt fountain have restricted the advance of the salt sheet, controlling geometrical variations in the namakiers (length, thickness, slope), enabling the development of a marginal namakier-dammed basin, and influencing current displacement rates.

The Mesijune salt fountain hosts a kilometre-scale supra-namakier basin filled with alluvium derived for the dissolutional erosion of the inclusion-rich extruded salt. This basin was formed in a trough related to restricted salt supply downstream of the bedrock-spur obstacle and associated with an encircling autosuture (i.e., merging of two salt lobes from the same feeder). The elongated shape of the basin and the overall offlap arrangement of its sedimentary fill, with older deposits in the distal sector, reflect the downslope expansion of the basin atop a laterally spreading namakier. The backtilting of the basin fill records differential vertical displacements attributable to variable patterns of extensional (thinning) and compressional (thickening) salt flow within a multidirectional namakier (i.e., radial spreading).

The advance of the NE front of the salt sheet blocked a drainage in the Late Pleistocene (pre-14 ka) creating marginal namakier-dammed basin with lacustrine-palustrine deposition. The obstruction of the salt glacier imposed by the relief induced a local compressional wave leading to greater salt build up and spreading in nearby areas, as recorded by disconnected residual Hormuz deposits.

This work presents for the first time comprehensive decomposed DInSAR data for a salt fountain in the Zagros Mountains at a mature and degraded stage. Previous studies were essentially focused on vigorously fed juvenile salt fountains. The highest horizontal displacement rates (ca. 140-100 mm/yr) occur on the steep and laterally unconfined flanks of the summit dome, with higher values in the sectors with greater local relief. The horizontal displacement rates decrease towards the distal edge of the namakier to a null value, suggesting a stable front. Vertical displacement rates in the summit dome (average −16 mm/yr) suggest that the salt fountain might evolve into a salt droplet in around 5 kyr, assuming constant surface lowering rates. Continuous degradation of the starved salt extrusion, including the dissolution of the salt, may result in a residual deposit dominated by cemented breccias (caprock) covering over 100 km^2. Similar breccias detected in the rock record may correspond to pointers of former extrusive salt sheets.

The Mesijune salt fountain serves as a terrestrial analogue that may help to understand the past evolution of salt sheets and associated features from the geological record (e.g., supra-salt basins, marginal basins, residual deposits).

CRediT authorship contribution statement

Francisco Gutiérrez: Conceptualization, Data curation, Formal analysis, Funding acquisition, Investigation, Methodology, Project administration, Resources, Software, Supervision, Validation, Visualization, Writing – original draft, Writing – review & editing. **Mahmud Haghshenas Haghighi:** Data curation, Writing – review & editing. **Issa Ilyati:** Data curation, Investigation, Writing – review & editing. **Mahdi Motagh:** Formal analysis, Writing – review & editing. **Miren del Val:** Formal analysis, Writing – review & editing. **Michael R. Hudec:** Formal analysis, Writing – review & editing. **Eduard Roca:** Formal analysis, Writing – review & editing. **Guillermo Pérez-Villar:** Investigation, Writing – review & editing.

Declaration of competing interest

The authors declare the following financial interests/personal relationships which may be considered as potential competing interests: Francisco Gutierrez reports financial support was provided by Spanish Government, Minsitry of Science, Innovation and Universities. If there are other authors, they declare that they have no known competing financial interests or personal relationships that could have appeared to influence the work reported in this paper.

Acknowledgements

The work has been supported by the Salvador de Madariaga grant (PRX22/00029) and projects DIAPERNO I and II (PID 2021-123189NB-I00, PID2025-167689NB-I00) of the Spanish Government (Ministerio de Ciencia, Innovación y Universidades). The TanDEM-X digital elevation models were provided by the German Aerospace Center (grant DEM-GEOL288). This work partially relied on InSAR Explorer for data analysis and visualization. The mayor of Chah Nar village, Mr. Darush Elhamyan, for generously providing logistical support. The authors are very grateful to Dr. Cathal Reilly (Midland Valley Exploration Ltd) and an anonymous reviewer for their insightful comments.

Appendix A. Supplementary data

Supplementary data to this article can be found online at https://doi.org/10.1016/j.marger.2026.207863.

Data availability

Data will be made available on request.

References

Abirifard, M., Raeisi, E., Zarei, M., Zare, M., Filippi, M., Bruthans, J., Talbot, C.J., 2017. Jahani salt Diapir, Iran: hydrogeology, karst features and effect on surrounding environment. Int. J. Speleol. 46, 445–457.

Aftabi, P., Roustaie, M., Alsop, G.I., Talbot, C.J., 2010. InSAR mapping and modelling of an active Iranian salt extrusion. J. Geol. Soc. 167, 155–170.

Agard, P., Omrani, J., Jolivet, L., Whitechuch, H., Vrielyck, B., Spakman, W., Monié, P., Meyer, B., Wortel, R., 2011. Zagros orogeny: a subduction-dominated process. Geol. Mag. 148, 692–725.

Aitken, M.J., Xie, J., 1990. Moisture correction for annual gamma dose. Anc. TL. 8, 6–9.

Barnhart, W.D., Lohman, R.B., 2012. Regional trends in active diapirism revealed by mountain range-scale InSAR time series. Geophys. Res. Lett. 39, L08309.

Berardino, P., Fornaro, G., Lanari, R., Sansosti, E., 2002. A new algorithm for surface deformation monitoring based on small baseline differential SAR interferograms. IEEE Trans. Geosci. Rem. Sens. 40, 2375–2383.

Berberian, M., 1995. Master "blind" thrust faults hidden under the Zagros folds: active basement tectonics and surface morphotectonics. Tectonophysics 241, 193–224.

Blair, T.C., McPherson, J.G., 1994. Alluvial fans and their natural distinction from rivers based on morphology, hydraulic processes, sedimentary processes, and facies assemblages. J. Sediment. Res. 64, 450–489.

Booth, J.R., Dean, M.C., DuVernay III, A.E., Styzen, M.J., 2003. Paleo-bathymetric controls on the stratigraphic architecture and reservoir development of confined fans in the Auger basin: central Gulf of Mexico slope. Marine and Petroleum Geology 20, 563–586.

Bosák, P., Jaros, J., Spudil, J., Sulovsky, P., Vaclavek, V., 1998. Salt plugs in the Eastern Zagros; Iran: results of regional geological reconnaissance. Geolines 7, 174.

Brennan, B.J., 2003. Beta doses to spherical grains. Radiat. Meas. 37, 299–303.

Brennan, B.J., Lyons, R.G., Phillips, S.W., 1991. Attenuation of alpha particle track dose for spherical grains. Int. J. Radiat. Appl. Instrum. Nucl. Tracks Radiat. Meas. 18, 249–253.

Bruthans, J., Asadi, N., Filippi, M., Vilhelm, Z., Zare, M., 2008. A study of erosion rates on salt diapir surfaces in the Zagros Mountains, SE Iran. Environmental Geology 53, 1079–1089.

Bruthans, J., Filippi, M., Asadi, N., Zare, M., Slechta, S., Churackova, Z., 2009. Surficial deposits on salt diapirs (Zagros Mountains and Persian Gulf platform, Iran): characterization, evolution, erosion and the influence on landscape morphology. Geomorphology 107, 195–209.

Bruthans, J., Filippi, M., Slavík, M., Závada, P., Zare, M., 2024. Rapid evolution of salt glacier caves on a Mountain diapir in a semiarid climate. Geomorphology 448, 109058.

Callot, J., Trocmé, V., Letouzey, J., Albouy, E., Jahani, S., Sherkati, S., 2012. Pre-existing salt structures and the folding of the Zagros Mountains. In: Alsop, G.I., Archer, S.G., Hartley, A.J., Grant, N.T., Hodgkinson, R. (Eds.), Salt Tectonics, Sediments and Prospectivity, 363. Geological Society, Special Publication, London, pp. 545–561.

Callot, J.P., Jahani, S., Letouzey, J., 2007. The role of pre-existing diapirs in fold and thrust belt development. In: Lacombe, O., Roure, F., Lavé, J., Vergés, J. (Eds.), Thrust Belts and Foreland Basins. Springer, Berlin, pp. 1–17.

Canova, D.P., Cofrade, G., Roca, E., DeMatheis, M., Ferrer, O., 2025b. Where the salt sheet ends-submarine allochthonous salt advance and hindrance, the Elda salt Sheet, Eastern Prebetics (Southern Iberia). Mar. Petrol. Geol., 107598

Canova, D.P., Roca, E., Ferrer, O., Ferrández-Cañadell, C., Escosa, F.O., Afzal, J., 2025a. From salt carapace to secondary minibasin encasement—The bolon Secondary Minibasin, Eastern External betics SE Iberia. Mar. Petrol. Geol., 107418

Clark, P.U., Shakun, J.D., Baker, P.A., Bartlein, P.J., Brewer, S., Brook, E., Carlson, A.E., Cheng, H., Kaufman, D.S., Liu, Z., Marchitto, T.M., 2012. Global climate evolution during the last deglaciation. Proc. Natl. Acad. Sci. 109, E1134–E1142.

Cofrade, G., Cantarero, I., Gratacós, Ó., Ferrer, O., Ramirez-Perez, P., Travé, A., Roca, E., 2023. Allochthonous salt advance recorded by the adjacent syn-kinematic sedimentation: example from the Les Avellanes diapir (South Central Pyrenees). Global Planet. Change 220, 104020.

De Waele, J., Gutiérrez, F., 2022. Karst Hydrogeology, Geomorphology and Caves. Wiley, Chichester.

del Val, M., Alonso, M.J., Duval, M., Arriolabengoa, M., Álvarez, I., Bodego, A., Cheng, H., Hermoso de Mendoza, A., Aranburu, A., Iriarte, E., 2022. Luminescence and ESR dating of the sedimentary infill from the multi-level cave system of Alkerdi-zelaieta (Navarre, N Spain). Quat. Geochronol. 73, 101380.

Dooley, T.P., Hudec, M.R., Jackson, M.P., 2012. The structure and evolution of sutures in allochthonous salt. AAPG (Am. Assoc. Pet. Geol.) Bull. 96, 1045–1070.

Dooley, T.P., Jackson, M.P.A., Hudec, M.R., 2009. Inflation a defletion of deeply buried salt stocks during lateral shortening. J. Struct. Geol. 31, 582–600.

Duffy, O., Hudec, M., Peel, F., Apps, G., Bump, A., Moscardelli, L., Dooley, T., Fernández, N., Bhattacharya, S., Wislan, K., Shuster, M., 2023. The role of salt tectonics in the energy transition: an overview and future challenges. Tektonika 1 (1).

Duller, G.A.T., 2008. Luminescence Dating. English Herit.

Durcan, J., King, G., Duller, G.A.T., 2015. DRAC: Dose rate and Age Calculator for trapped charge dating. Quat. Geochronol. 28, 54–61.

Ezati Asl, M., Faghih, A., Mukherjee, S., Soleimany, B., 2019. Style and timing of salt movement in the Persian Gulf basin, offshore Iran: insights from halokinetic sequences adjacent to the Tonb-e-Bozorg salt diapir. J. Struct. Geol. 122, 116–132.

Fattahi, H., Amelung, F., 2013. DEM error correction in InSAR time series. IEEE Trans. Geosci. Rem. Sens. 51, 4249–4259.

Galbraith, R.F., Roberts, R.G., Laslett, G.M., Yoshida, H., Olley, J.M., 1999. Optical dating of single and multiple grains of quartz from Jinmium rock shelter, Northern Australia: part 1, experimental design and statistical models. Archaeometry 41, 339–364.

Ghassemi, M.R., Roustaei, M., 2021. Salt extrusion kinematics: insights from existing data, morphology and InSAR modelling of the active emergent Anguru diapir in the Zagros fold and thrusy belt, Iran. J. Geol. Soc. 178, gs2020–g2136.

Goldstein, R.M., Werner, C.L., 1998. Radar interferogram filtering for geophysical applications. Geophys. Res. Lett. 25, 4035–4038.

Guérin, G., Mercier, N., Adamiec, G., 2011. Dose-rate conversion factors: update. Ancient TL 29, 5–8.

Guérin, G., Mercier, N., Nathan, R., Adamiec, G., Lefrais, Y., 2012. On the use of the infinite matrix assumption and associated concepts: a critical review. Radiat. Meas. 47, 778–785.

Gutiérrez, F., Deirnik, H., Zarei, M., Medialdea, A., 2023a. Geology, geomorphology and geochronology of the coseismic? Emad Deh rock avalanche associated with a growing anticline and a rising salt diapir, Zagros Mountains, Iran. Geomorphology 421, 108527.

Gutiérrez, F., Haghigi, M.H., Ilyati, I., Motagh, M., del Val, M., 2025b. Diapiric and tectonic geomorphology of the river-damming Jahani salt extrusión associated with the strike-slip Kareh Bas fault, including DinSAR displacement data (Zagros Mountains, Iran. Geomorphology 488, 109955.

Gutiérrez, F., Ilyati, I., Pérez-Villar, G., 2026. The geomorphology of the mature, fluviokarst-dominated Mesijune salt extrusion (Zagros Mountain, Iran). Insights into the evolution of salt fountains. Geomorphology submitted for publication.

Gutiérrez, F., Ilyati, I., Rezaei, M., Zarei, M., Hudec, M., 2024. Active strike-slip faulting, diapirism and seismic hazards. The case of the Kareh Bas fault and the associated Dandenjan salt extrusion in the zagros Mountains, SW Iran. J. Struct. Geol. 187, 105239.

Gutiérrez, F., Ilyati, I., Zarei, M., 2025a. Surface karst geomorphology in the Jahani salt extrusion, Zagros Mountains, Iran. Geomorphology 485, 109859.

Gutiérrez, F., Zarei, M., Hudec, M.R., Deirnik, H., 2023b. Normal faulting and landsliding in morpho-structural domes related to buried salt stocks, Zagros Mountains, Iran. Insights into salt breakout. Mar. Petrol. Geol. 155, 106376.

Harrison, J.V., 1930. The geology of some salt-plugs in Laristan, southern Persia. Quarterly Journal of the Geological Society 86, 463–522.

Hassanpour, J., Jahani, S., Ghassemi, M.R., Alavi, S.A., Zeinali, F., 2018. Evolution of the Karebas fault System and adjancent folds, central Zagros fold-and-thrust belt, Iran: role of pre-existing halokinesis (salt structures and minibasins) and detachment levels. J. Asian Earth Sci. 164, 125–142.

Hearon IV, T.E., Rowan, M.G., Giles, K.A., Kernen, R.A., Gannaway, C.E., Lawton, T.F., Fiduk, J.C., 2015. Allochthonous salt initiation and advance in the northern Flinders and eastern Willouran ranges, South Australia: using outcrops to test subsurface-based models from the northern Gulf of Mexico. AAPG (Am. Assoc. Pet. Geol.) Bull. 99, 293–331.

Hessami, K., Koyi, H.A., Talbot, C.J., Tabasi, H., Shabanian, E., 2001. Progressive unconformities within an evolving foreland fold–thrust belt, Zagros Mountains. J. Geol. Soc. 158, 969–981.

Hogenson, K., Kristenson, H., Kennedy, J., Johnston, A., Rine, J., Logan, T., Zhu, J., Williams, F., Herrmann, J., Smale, J., Meyer, F., 2020. Hybrid Pluggable Processing Pipeline (HyP3): A cloud-native infrastructure for generic processing of SAR data [Computer software]. https://doi.org/10.5281/zenodo.4646138.

Hudec, M.R., Jackson, M.P.A., Schultz-Ela, D.D., 2009. The paradox of minibasin subsidence into salt: clues to the evolution of crustal basins. Geol. Soc. Am. Bull. 121, 201–221.

Hudec, M.R., Jackson, M.P.A., 2006. Advance of allochthonous salt sheets in passive margins and orogens. AAPG (Am. Assoc. Pet. Geol.) Bull. 90, 1535–1564.

Jackson, M.P.A., Hudec, M.R., 2017. Salt Tectonics. Principles and Practice. Cambridge University Press, Cambridge.

Jahani, S., Callot, J.P., Frizon de Lamotte, D., Letouzey, J., Leturmy, P., 2007. The salt diapirs of the eastern Fars Province (Zagros, Iran): a brief outline of their past and present. In: Lacombe, O., Roure, F., Lavé, J., Vegés, J. (Eds.), Thrust Belts and Foreland Basins. Springer, Berlin, pp. 289–308.

Jahani, S., Callot, J.P., Letouzey, J., Frizon de Lamotte, D., 2009. The eastern termination of the Zagros fold-and-thrust Belt, Iran: structures, evolution, and relationships between salt plugs, folding, and faulting. Tectonics 28. TC6004.

Jahani, S., Hassanpour, J., Mohammadi-Firouz, S., Letozey, J., de Lamotte, D.F., Alavi, S. A., Soleimany, B., 2017. Salt tectonics and tear faulting in the central part of the Zagros fold-Thrust Belt, Iran. Mar. Petrol. Geol. 86, 426–446.

Kent, P.E., 1958. Recent studies of South Persian salt plugs. AAPG (Am. Assoc. Pet. Geol.) Bull. 42, 2951–2972.

Kent, P.E., 1979. The emergent Hormuz salt plugs of southern Iran. J. Petrol. Geol. 2, 117–144.

Kergaravat, C., Ribes, C., Legeay, E., Callot, J.-P., Kavak, K.S., Ringenbach, J.-C., 2016. Minibasins and salt canopy in foreland fold-and-thrust belts: the central Sivas basin, Turkey. Tectonics 35, 1342–1366.

Leach, D.L., Taylor, R.D., Fey, D.L., Diehl, S.F., Saltus, R.W., 2010. A deposit model for Mississippi Valley-type lead-zinc ores. In: Mineral Deposit Models for Resource Assessment. USGS Geological Survey. Scientific Investigations Report 2010–5070-A. http://www.usgs.gov/pubprod.

Letouzey, J., Sherkati, S., 2004. Salt movement, tectonic events, and structural style in the central Zagros fold and thrust belt (Iran). In: 24th Annual GCSSEPM Foundation. Bob F. Perkins Research Conference: Salt-Sediment Interactions and Hydrocarbon Prospectivity: Concepts, Applications, and Case Studies for the 21st Century, Gulf Coast Section. Society for Sedimentary Geology, Houston, Texas.

Masibeygi, M., 1965. Chahgheyb Geological Map, 1:100,000 Scale. National Iranian Oil Company.

Molinaro, M., Leturmy, P., Guezou, J.C., Frizon de Lamotte, D., Eshraghi, S.A., 2005. The structure and kinematics of the southeastern Zagros fold-thrust belt, Iran: from thin-skinned to thick-skinned tectonics. Tectonics 24. TC3007.
Mouthereau, F., Lacombe, O., Meyer, B., 2006. The Zagros folded belt (Fars, Iran): constraints from topography and critical wedge modelling. Geophys. J. Int. 165, 336–356.
Mouthereau, F., Tensi, J., Bellahsen, N., Lacombe, O., De Boisgrollier, T., Kargar, S., 2007. Tertiary sequence of deformation in a thin-skinned/thick-skinned collision belt: the Zagros folded belt (fars, Iran). Tectonics 26. TC5006.
Murray, A.S., Wintle, A.G., 2000. Luminescence dating of quartz using an improved single-aliquot regenerative-dose protocol. Radiat. Meas. 37, 377–381.
Murray, A.S., Wintle, A.G., 2003. The single aliquot regenerative dose protocol: potential for improvements in reliability. Radiat. Meas. 32, 57–73.
NIOC, 1977. Darab Geological Compilation Map, 1:250,000 Scale. National Iranian Oil Company.
Noroozi, M.H., 1966. Chahar Berkeh Geological Map, 1:100,000 Scale. National Iranian Oil Company.
O'Brien, J.J., Lerche, I., 1988. Impact of heat flux anomalies around salt diapirs and salt sheets in the Gulf Coast on hydrocarbon maturity: models and observations. Trans. Gulf Coast Assoc. Geol. Soc. 38, 231–243.
Orang, K., Hossein, M., Azadikhah, A., Royatvand, M., 2017. Structural framework and tectono-stratigraphic evolution of the easten Persian Gulf, offshore Iran. Mar. Petrol. Geol. 91, 89–107. https://doi.org/10.1016/j.marpetgeo.2017.12.014.
Pepe, A., Lanari, R., 2006. On the extension of the minimum cost flow algorithm for phase unwrapping of multitemporal differential SAR interferograms. IEEE Trans. Geosci. Rem. Sens. 44, 2374–2383.
Perona, J., Canals, À., Cardellach, E., 2018. Zn-Pb Mineralizations associated with salt diapirs in the basque-cantabrian basin (N Spain): geology, geochemistry and genetic model. Econ. Geol. 113, 1133–1159.
Perry, J.T.O.'B., Setudehnia, A., Nasr, M., 1965. SE Fars Geological Compilation Map , 1: 250,000 Scale. Iranian Oil Operating Companies.
Prescott, J.R., Hutton, J.T., 1994. Cosmic ray contributions to dose rates for luminescence and ESR dating: large depths and long term time variations. Radiat. Meas. 23, 497–500.
Pérez-Villar, G., Gutiérrez, F., Benito-Calvo, A., Roqué, C., 2025. Morphometry and spatio-temporal evolition of salt karren. Earth Surf. Process. Landf. 50, e70119.
Pérez-Villar, G., Gutiérrez, F., Benito-Calvo, A., Roqué, C., 2026. Erosion rates in rock salt exposures with diverse karren monitored by erosion pins, close-range photogrammetry and terrestrial laser scanner. Geomorphology, 110228.
Raymond, J., Langevin, H., Comeau, F.-A., Malo, M., 2022. Temperature dependence of rock salt thermal conductivity: implications for geothermal exploration. Renew. Energy 184, 26–35.
Ricou, L.E., Braud, J., Brunn, J.H., 1977. Le Zagros. Mem. Soc. Geol. Fr. 8, 33–52.
Rowan, M.G., Hearon IV, T.E., Kernen, R.A., Giles, K.A., Gannaway-Dalton, C.E., Williams, N.J., Fiduk, J.C., Lawton, T.F., Hannah, P.T., Fischer, M.P., 2020. A review of allochthonous salt tectonics in the flinders and willouran ranges, South Australia. Aust. J. Earth Sci. 67, 787–813.
Ruh, J.B., Hirt, A.M., Burg, J.P., Mohammadi, A., 2014. Forward propagation of the Zagros simply Folded Belt constrained from magnetostratigraphy of growth strata. Tectonics 33, 1534–1551.
Sedaghat, M.E., Kashani, F., Allahmadadi, S., 2005. Bezanjan Geological Map, 1:100,000 Scale. Geological Survey and Mineral Exploration of, Iran.
Sepehr, M., Cosgrove, J.W., 2004. Structural framework of the Zagros fold–thrust belt, Iran. Mar. Petrol. Geol. 21, 829–843.
Sepehr, M., Cosgrove, J.W., 2005. Role of the Kazerun fault zone in the formation and deformation of the zagros fold-thurst belt, Iran. Tectonics 24. TC5005.
Shami, S., Shahriari, M.A., Nilfouroushan, F., Forghani, N., Salimi, M., Reshadi, M.A.M., 2024. Surface displacement measurement and modelling of the Shah-Gheyb salt dome in southern Iran using InSAR and machine learning techniques. Int. J. Appl. Earth Obs. Geoinf. 132, 104016.
Simmons, G.R., 1992. The Regional Distribution of Salt in the Northwestern Gulf of Mexico: Styles of Emplacement and Implications for Early Tectonic History. Texas A&M University, College Station, Texas, p. 180. Ph. D Thesis.
Smith, R., 2004. Silled sub-basins to connected tortuous corridors: sediment distribution systems on topographically complex subaquaeous slopes. In: Lomas, S.A., Joseph, P. (Eds.), Confined Turbidite Systems, 222. Geological Society, Special Publication, Londong, pp. 23–43.
Snidero, M., Muñoz, J.A., Carrera, N., Butillé, M., Mencos, J., Motamedi, H., Piryaei, A., Sàbat, F., 2019. Temporal evolution of the Darmadan salt diapir, eastern Fars region, Iran. Tectonophysics 766, 115–130. https://doi.org/10.1016/j.tecto.2019.06.006.
Snidero, M., Muñoz, J.A., Santolaria, P., Carrera, N., Butillé, M., 2025. Structural evolution of the Handun salt diapir, Zagros fold and thrust belt, southern Iran. Mar. Petrol. Geol. 171, 107172. https://doi.org/10.1016/j.marpetgeo.2024.107172.
Soleimani, M., Nadimi, A., Koltai, G., Dublyansky, Y., Carolin, S., Spötl, C., 2023. Stalagmite evidence of last Glacial Maximum to early Holocene climate variability in Southwestern Iran. J. Quat. Sci. 38, 308–318.
Stöcklin, J., 1968. Structural history and tectonics of Iran: a review. Am. Assoc. Petrol. Geol. Bull. 52, 1229–1258.
Talbot, C.J., 1979. Fold trains in a glacier of salr in southern Iran. J. Struct. Geol. 1, 5–18.
Talbot, C.J., Alavi, M., 1996. The past of a Future Syntaxis Across the Zagros, 100. Geological Society, London, Special Publication, pp. 89–109.
Talbot, C.J., Jarvis, R.J., 1984. Age, budget and dynamics of an active salt extrusion in Iran. J. Struct. Geol. 6, 521–533.
Talbot, C.J., Pohjola, V., 2009. Subaerial salt extrusions in Iran as analogues of ice sheets, streams and glaciers. Earth Sci. Rev. 97, 155–183.
Talbot, C.J., Rogers, E.A., 1980. Seasonal movements in a salt glacier in Iran. Science 208, 395–397.
Tomás, R., Pastor, J.L., Gutiérrez, F., Navarro-Hernández, M.I., Riquelme, A., Cano, M., Liu, X., 2026. Detecting and assessing salt dissolution-induced subsidence in an urban area using open-access remote-sensed data (Monóvar, SE Spain). Eng. Geol. submitted for publication.
Vendeville, B.C., Jackson, M.P.A., 1992. The fall of diapirs during thin-skinned extension. Mar. Petrol. Geol. 9, 354–371.
Vernant, P., Nilforoushan, F., Hatzfeld, D., Abbassi, M.R., Vigny, C., Masson, F., Nankali, H., Martinod, J., Ashtiani, A., Bayer, R., Tavakoli, F., Chéry, J., 2004. Present-day crustal deformation and plate kinematics in the Middle East constrained by GPS measurements in Iran and northern Oman. Geophys. J. Int. 157, 381–398.
Warren, J.K., 2006. Evaporites: Sediments, Resources and Hydrocarbons. Springer-Verlag.
Warren, J.K., 2016. Evaporites: a Geological Compendium. Springer, Dordrecht.
Warren, J.K., 2017. Salt usually seals, but sometimes leaks: implications for mine and cavern stabilities in the short and long term. Earth Sci. Rev. 165, 302–341.
Wessel, B., 2016. TanDEM-X ground segment – DEM products specification document. EOC, DLR, Oberpfaffenhofen, Germany, Public Document TD-GS-PS-0021 1–46 [Online]. Available:, Issue 3.2, 2016. https://tandemx-science.dlr.de/.
Wright, T.J., Parsons, B.E., Lu, Z., 2004. Toward mapping surface deformation in three dimensions using InSAR. Geophys. Res. Lett. 31, L01607.
Yunjun, Z., Fattahi, H., Amelung, F., 2019. Small baseline InSAR time series analysis: unwrapping error correction and noise reduction. Comput. Geosci. 133, 104331.
Zarei, M., Raeisi, E., Talbot, C., 2012. Karst development on a mobile substrate: konarsiah salt extrusion, Iran. Geol. Mag. 149, 412–422.
Zarei, M., Raeisi, E., 2010. Karst development and hydrogeology of Konarsiah salt diapir, south of Iran. Carbonates Evaporites 25, 217–229.
Zebari, M., Friedrich, A., Rieger, S.M., Plattner, C., Bruthans, J., Závada, P., Kahle, B., Parizzi, A., 2025. Surface deformation and salt budget of an active salt fountain, Finu un the Zagros Mountains, Iran, using persistent scatterer interferometry. Lithosphere 3 lithosphere_2024_216.
Zhang, S., Jiang, Q., Shi, C., Xu, X., Gong, Y., Xi, J., Liu, W., Liu, B., 2021. Application of Sentinel-1 and -2 images in measuring the deformation of Kuh-e-Namak (Dashti) namakier, Iran. Rem. Sens. 13, 785.
Zhang, Q., Alves, T., 2024. Contrasting influence of salt structures and faults on the geothermal potential of regional structural highs: the Cleaver bank high, Southern North Sea. Geothermics 116, 102842.